

See discussions, stats, and author profiles for this publication at: <https://www.researchgate.net/publication/360054868>

A Novel Fusion Method for Generating Surface Soil Moisture Data With High Accuracy, High Spatial Resolution, and High Spatio-Temporal Continuity

Article in *Water Resources Research* · May 2022

DOI: 10.1029/2021WR030827

CITATIONS

22

READS

1,117

11 authors, including:



Shuzhe Huang
Wuhan University

15 PUBLICATIONS 207 CITATIONS

SEE PROFILE



Zhang Xiang
China University of Geosciences

132 PUBLICATIONS 3,425 CITATIONS

SEE PROFILE



Nengcheng Chen
Wuhan University

236 PUBLICATIONS 4,191 CITATIONS

SEE PROFILE



Hongliang Ma
University of Copenhagen

43 PUBLICATIONS 818 CITATIONS

SEE PROFILE

A Novel Fusion Method for Generating Surface Soil Moisture Data with High Accuracy, High Spatial Resolution, and High Spatio-Temporal Continuity

Shuzhe Huang ^a, Xiang Zhang ^{b,*}, Nengcheng Chen ^b, Hongliang Ma ^a, Peng Fu ^{c,d}, Jianzhi Dong ^e, Xihui Gu ^{f,g}, Won-Ho Nam ^h, Lei Xu ^{a,b}, Gerhard Rab ^{i,j}, Dev Niyogi ^k

^a State Key Laboratory of Information Engineering in Surveying, Mapping, and Remote Sensing (LIESMARS), Wuhan University, Wuhan 430079, China.

^b National Engineering Research Center of Geographic Information System, School of Geography and Information Engineering, China University of Geosciences (Wuhan), Wuhan, 430074, China.

^c Carl R. Woese Institute for Genomic Biology, University of Illinois at Urbana-Champaign, Urbana, IL, USA.

^d Department of Plant Biology, University of Illinois at Urbana-Champaign, Urbana, IL, USA.

^e Department of Civil and Environmental Engineering, Massachusetts Institute of Technology, Cambridge, Massachusetts, USA

^f Department of Atmospheric Science, School of Environmental Studies, China University of Geosciences, Wuhan 430074, China.

^g School of Geography and the Environment, University of Oxford, Oxford OX1 3QY, UK

^h School of Social Safety and Systems Engineering, Institute of Agricultural Environmental Science, National Agricultural Water Research Center, Hankyong National University, Anseong, Republic of Korea

ⁱ Institute of Hydraulic Engineering and Water Resources Management, University of Technology Vienna, Austria

^j Institute for Land and Water Management Research, Federal Agency for Water Management, Petzenkirchen, Austria

This article has been accepted for publication and undergone full peer review but has not been through the copyediting, typesetting, pagination and proofreading process, which may lead to differences between this version and the [Version of Record](#). Please cite this article as [doi: 10.1029/2021WR030827](#).

This article is protected by copyright. All rights reserved.

^kDepartment of Geological Sciences, Jackson School of Geosciences, and Department of Civil, Architecture, and Environmental Engineering, University of Texas at Austin, Austin, TX 78712, USA.

* Corresponding author: Dr. Xiang Zhang (zhangxiang76@cug.edu.cn)

Key Points:

- The proposed framework applied point-surface data fusion through deep learning.
- 30 m seamless surface soil moisture (SSM) with high accuracy was generated.
- Downscaled SSM showed good agreement with in-situ SSM observations.

Abstract

Surface soil moisture (SSM) has a considerable impact on land-atmosphere exchanges of water and energy fluxes. However, due to the inherent deficiencies of remotely sensed data (e.g., cloud contamination in thermal remote sensing, coarse resolutions for microwave remote sensing), none of the current algorithms alone can provide daily and seamless field-scale (30 m) SSM information. To fill the gap, we proposed a novel SSM fusion framework to Generate high Resolution, Accurate, Seamless data using Point-Surface fusion (GRASPS) based on remotely sensed, reanalysis, and in-situ datasets. First, 30 m seamless continuous SSM correlated variables (land surface temperature, NDVI, and albedo) were downscaled by enhanced spatial and temporal adaptive reflectance fusion model (ESTARFM). Then, downscaled auxiliary variables and other background variables were input into a deep learning model to produce 30 m daily and seamless SSM fields. To further improve the SSM estimation accuracy, a pixel classification based bias correction method was developed. The GRASPS method was validated over an in-situ soil moisture sensor network (HOAL network) in Austria. The average Pearson correlation coefficient (PCC), root mean squared error (RMSE), unbiased RMSE (ubRMSE), bias, and mean absolute error (MAE) over all validation sites achieved 0.78, $0.048 \text{ m}^3\text{m}^{-3}$, $0.033 \text{ m}^3\text{m}^{-3}$, -0.001

m^3m^{-3} , and $0.041\ m^3m^{-3}$, respectively. After bias correction, RMSE, ubRMSE, bias, and MAE decreased by 13%, 7%, 22%, and 18%, respectively. The proposed method maximizes the potential of data fusion and deep learning in generating field-scale seamless SSM, which is promising for fine-scale studies and applications in agricultural, hydrological, and environmental domains.

Keywords: Surface soil moisture, Point-surface data fusion, Deep learning

1. Introduction

Surface soil moisture (SSM) has been identified as an "Essential Climate Variable" in the Global Climate Observing System. It is one of the most significant land surface variables and plays a critical role in monitoring and understanding the global environment and climate change (Bojinski et al., 2014; McColl et al., 2017). Although soil holds only a tiny fraction of water on the globe (e.g., compared to sea, lake etc.), a long-term and spatio-temporally consistent soil moisture dataset is of critical importance for studies in water resources management, ecosystem modeling, human health, and extreme weather events including floods and droughts (Dorigo et al., 2017; Wang et al., 2022; Huang et al., 2021; Koster et al., 2004). Over the last decades, SSM is mainly obtained by ground sensor networks and remote sensing satellites. In-situ SSM sensor networks have the strength in providing long-term, stable, and accurate (compared to satellite-based and model-based soil moisture products) soil moisture data, but the costly maintenance and sparse distribution make it difficult to quantify regional heterogeneity of SSM (Arabi et al., 2020; Wu et al., 2020). Alternatively, several Earth-orbiting satellite missions dedicated to SSM have been launched in this century and many remotely sensed SSM products have been provided (Entekhabi et al., 2010; Kerr et al., 2010; Njoku et al., 2003; Wagner et al., 2013; Wigneron et al., 2021). Passive microwave can measure land surface natural emissions of soil (i.e., thermal microwave radiation from soils) with high temporal resolution (e.g., daily) and spatial continuity while active microwave sensors are superior in spatial resolution such as the 3 km Soil

Moisture Active Passive (SMAP) SSM product based on active radar (Kim et al., 2020; Ma et al., 2019; Wang et al., 2018;). At present, optical satellite images are usually adopted to generate SSM observations at high spatial resolutions (tens of meters). However, cloud contamination and atmospheric pollution usually prevent producing spatio-temporally continuous remotely sensed SSM (Cheng et al., 2014; Liu et al., 2021).

Generally speaking, the current point-wise (ground sensor network) and surface-based (satellite or airborne) approaches have diverse and complementary capabilities in SSM monitoring/estimation (Chen et al., 2021). Specifically, in-situ SSM can provide accurate and stable SSM values while satellite-based and model-based SSM products can provide SSM values at regional to global scale. However, neither of them alone can obtain SSM with High accuracy, High spatial resolution, and High spatio-temporal continuity (cloud-free and daily) simultaneously (referred to as 3H data). 3H SSM data is of great significance for soil moisture based environmental applications. Nevertheless, utilizing downscaling techniques to obtain 3H SSM is still a big challenge (Ford et al., 2019; Kathuria et al., 2019; Peng et al., 2017;).

The primary studies in the SSM downscaling concern satellite-based data fusion methods, which usually combine microwave or optical/thermal soil moisture products to obtain SSM with high spatial resolution or high spatial consistency. The typical combinations of remote sensors include active and passive microwave data fusion, optical/thermal and microwave data fusion (Das et al., 2014; Hu et al., 2020; Li et al., 2018). For example, Song et al. (2021) developed a non-linear enhanced soil moisture downscaling model and downscaled the originally 25 km passive microwave SSM products (Advanced Microwave Scanning Radiometer-2, AMSR-2) to 1 km by fusing multiple optical remote sensing data. Das et al. (2019) merged the passive microwave-based SMAP product with active microwave-based Sentinel-1 data. Validations at 1 km and 3 km showed a reasonable accuracy. Model-based downscaling frameworks have also been developed to further integrate the physical process and address the transferability (De Lannoy and Reichle et al., 2016; Lievens et al., 2016; Senanayake et al., 2019). For instance, Vergopolan et al. (2020) combined a radiative transfer model

(RTM) and a hyper-resolution land surface model (LSM) with a Bayesian scheme and finally generated SSM estimations at 30 m. The downscaled SSM was confirmed to feasibly capture the spatio-temporal dynamics of SSM at field scale with more spatial details compared to original passive soil moisture products.

The second kind of technique in SSM downscaling is to build data assimilation methods based on global hydrological models (GHMs) or LSMs. There are also several model-based reanalysis data sets published in recent decades. As a typical example, the China Meteorological Administration Land Data Assimilation System (CLDAS) adopted various LSMs and integrated multiple forcing variables (e.g., precipitation, temperature) to produce assimilated SSM with a spatial resolution of 0.0625° (Wang et al., 2021). Besides, the ERA-5 product assimilates various satellite data, in-situ measurements, and model-based data to generate global SSM data at 0.1° spatial resolution (Hersbach et al., 2020).

In most recent years, more and more attempts have been made to downscale SSM by incorporating other SSM-related land surface variables (e.g., NDVI and precipitation). Previous studies found that SSM correlated land surface variables, such as vegetation characteristics, meteorological factors, and topography, could be adopted within the SSM downscaling (Kolassa et al., 2018; Piles et al., 2011). Therefore, a series of statistical algorithms have been used to produce high-resolution SSM. Particularly, machine learning methods including random forest (RF), support vector machine (SVM), and artificial neural networks (ANN) were adopted to downscale and estimate SSM due to its powerful ability to fit a non-linear relationship between independent and dependent variables (Liu et al., 2020; Peng et al., 2021; Xu et al., 2018). For example, Wei et al. (2019) applied gradient boosting decision tree regression and a total of 26 SSM related indices to downscale 36 km SMAP SSM to 1 km over the Tibetan Plateau, China. Abbaszadeh et al. (2018) enhanced SMAP SSM to 1 km over the CONUS using the RF model by considering the soil texture characteristics.

Despite the great achievements of the above studies, there are still some major limitations for realizing 3H SSM data retrieval (Xu et al., 2021). First, the majority of existing studies focused on the surface-surface based SSM data fusion, while point-

Accepted Article

surface (i.e., ground-space) data fusion is still in its infant stage (Montzka et al., 2016; Shen et al., 2019; Zhang et al., 2021). Although surface-surface fusion can produce large-scale SSM data by adopting areal products (satellite-based or model-based SSM data) as model output, the scale mismatch issue of coarse resolution and field-scale resolution products may introduce merging errors and losses of spatial information (Piles et al., 2011). In this case, it is natural to consider the combination of point-wise data (in-situ ground measurements) and areal products, which have complementary advantages in providing SSM (Montzka et al., 2016; Yuan et al., 2020b; Zhang et al., 2018). More importantly, previous studies mostly targeted one or two aspects of the SSM improvements, such as either spatial and temporal resolution or temporal continuity (Cui et al., 2016; Qu et al., 2019; Qu et al., 2021). Particularly, traditional downscaling algorithms often ignored the spatial consistency (i.e., cloud-free) of SSM. However, without field scale 3H SSM data, fine-scale environmental and hydrological modeling as well as agricultural management cannot be easily achieved (Abowarda et al., 2021; Gu et al., 2019). To this point, a framework that can produce 3H SSM data (i.e., high resolution, high spatio-temporal continuity, and high accuracy) is still urgently required. Finally, as the new generation of technology in machine learning, deep learning has been confirmed to be a promising technique in numerous domains and outperforms the traditional machine learning algorithms with substantial improvement in performance (Li et al., 2021a; Li et al., 2021b; Shen et al., 2020; Yuan et al., 2020a). However, to what extent deep learning can aid in enhancing the quality of downscaled SSM remains unclear.

To address the above issues, the main objective of this study is to propose a complete and advanced SSM fusion framework by applying a point-surface data fusion framework based on deep learning. We aim to generate robust field-scale (30 m) spatio-temporally continuous (daily) SSM. The proposed method will shed light on the 3H SSM data generation method, which may improve our understandings in environmental change, precision agriculture and water management. Meanwhile, the proposed methodology also has the potential to be used for other land surface variables (e.g., air temperature, evapotranspiration, precipitation) at different spatial resolutions (e.g., 1

km, 0.1°). Thus, this study has much broader implications for remote sensing-based environmental research.

2. Study Area and Data

2.1 Study Area

The study area is located in Petzenkirchen, Austria (48°9'N, 15°9'E), covering an area of about 400 ha (Fig. 1). A soil moisture network is operated here in an agricultural catchment named Hydrological Open Air Laboratory (HOAL), which provides in-situ soil moisture data to the International Soil Moisture Network (ISMN). The experimental catchment is established to provide a wide range of data for advancing the understanding of water-related transport processes (e.g., runoff, sediments, and nutrients), catchment evapotranspiration, and soil moisture patterns (Chen et al., 2020; Pfeil et al., 2018). The entire area is characterized by a temperate and humid climate, with mean annual precipitation around 800 mm/year and mean annual temperature of 10°C over last two decades. The temperature and rainfall amount are higher in summer and lower in winter. With an elevation ranging from 253 to 325 m above sea level, more than sixty percent of the total study area is dominated by agricultural lands, while the remaining catchment is mainly forested, paved or used as pasture (Széles et al., 2021). The primary soil types in this area are Cambisols, Kolluvisol, Planosols, and Gleysols, with medium to poor infiltration capacities. Due to the local climate and soil condition, there are two major crop growing seasons in HOAL. Summer crops (dominated by maize) are usually sown in April and harvested in October. Winter crops (e.g., wheat) are commonly planted in November and reaped in June of the following year (Tiefenbacher et al., 2021; Xaver et al., 2020). Depending on the weather and crop growing status, sown dates may change by several weeks. In the HOAL soil moisture network, 24 in-situ soil moisture sensors equipped with wireless transmission technology were set up. A part of the sensors was placed permanently and have continuous data records while the remaining are temporarily removed each year for

several months due to the local field management practices. Given the local climate patterns, land cover, agricultural features, and sensor distribution, the HOAL catchment is ideal for testing the soil moisture downscaling method.

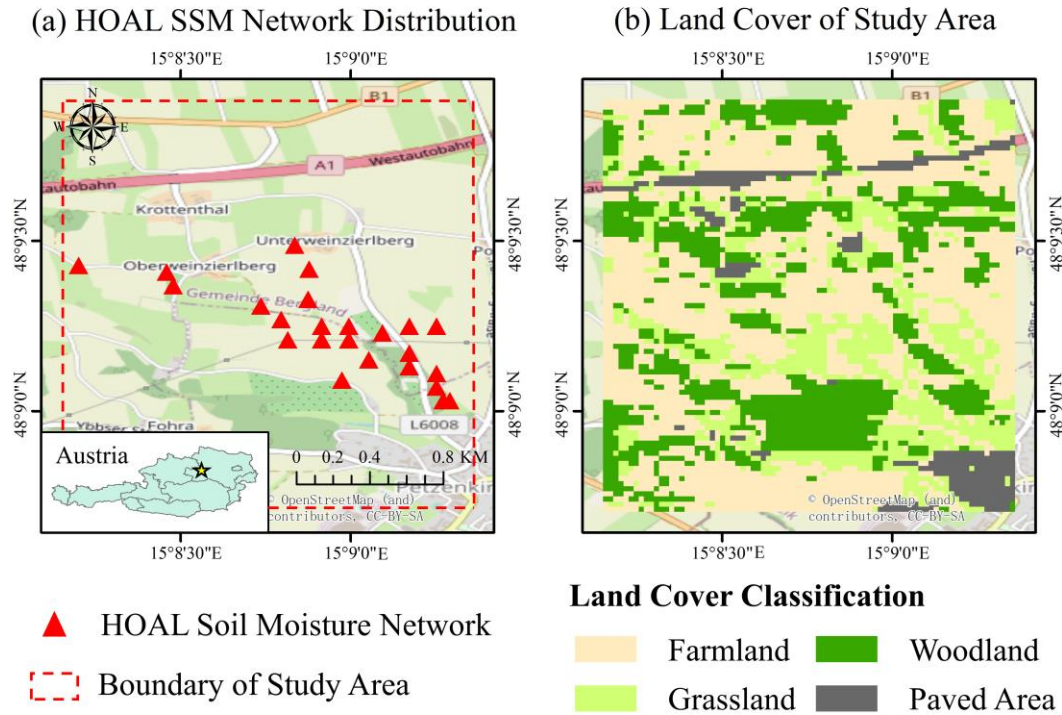


Fig. 1. The overview of the study area. (a) shows the spatial distribution of soil moisture sensors in the HOAL network. (b) shows the major land cover types in the study area.

2.2 Datasets

In this study, a total of three categories of datasets were adopted for generating 30 m spatio-temporally continuous soil moisture (Table 1). Specifically, the data sets contained: (1) remotely sensed products including Landsat 8, MOD11A1, MOD09GA; (2) model-based products including SMAP Level-4 SSM and the ERA-5 reanalysis product; (3) ISMN in-situ soil moisture measurements. Detailed information of these data sources was given in the following subsections.

Table 1 The descriptions of data sets used in this study.

Category	Product	Variable	Spatial Resolution	Temporal Resolution
Remotely sensed	Landsat 8	Surface Reflectance	30 m	16 Days
		Thermal Infrared	100 m	
Surface Data	MOD11A1	Land Surface Temperature	1 km	Daily
	MOD09GA	Surface Reflectance	500 m	Daily
Model-based Data	ERA-5	Volumetric Soil Water		
		Total Precipitation	0.1°	Hourly
		Skin Temperature		
	SMAP Level4	Surface Soil Moisture	9km	3 hours
In-situ Data	ISMN HOAL network	Surface Soil Moisture (0~5cm)	--	Hourly

2.2.1 Remotely Sensed Products

Launched in 2013, Landsat 8 is the seventh orbiting satellite in the Landsat series (Markham et al., 2012). The satellite is equipped with two major instruments: Operational Land Imager (OLI) and Thermal Infrared Sensor (TIRS). In this study, Landsat 8 data was acquired from Google Earth Engine (GEE), and the clear sky images (i.e., cloud cover $\approx 0\%$) were selected based on the cloud information using GEE. Here the thermal infrared bands (~ 100 m) have been resampled to 30 m using cubic convolution. The visible and infrared bands (1-7) were further used to calculate NDVI and Albedo. The thermal infrared bands were used to retrieve Landsat land surface temperature (LST) based on an open-source single-channel framework on GEE (Wang et al., 2020).

Moderate Resolution Imaging Spectroradiometer (MODIS) is the primary instrument aboard the Terra and Aqua satellites (Vermote and Wolfe, 2015). In this study, the daily 500 m MODIS surface reflectance product (MOD09GA) and the daily 1 km MODIS LST product (MOD11A1) were collected from a free data platform named the Application for Extracting and Exploring Analysis Ready Samples (AppEEARS; lpdaac.usgs.gov/tools/appeears/). Here only daytime (overpass time ranging from 10:00 am to 12:00 am at local time) LSTs were chosen for the SSM downscaling. These products also contain quality control (QC) information describing cloud state and data quality. We used QC information to exclude the pixels affected by cloud cover or cloud shadow. For LST, only the pixels with good quality or LST retrieval errors lower than 1 K were chosen. To match the projection with other products in the current research, the MOD09GA and MOD11A1 were reprojected to UTM projection with WGS84 datum by ArcGIS.

2.2.2 Model-based Products

Developed by the National Aeronautics and Space Administration (NASA), the SMAP satellite was launched on 31 January 2015. In this study, SMAP Level-4 (SMAP L4), a land assimilation-based soil moisture product, was adopted as one of the soil moisture background data (Reichle et al., 2017), which integrates lower-level SMAP product and model estimates from a land surface model (LSM) in a data assimilation system. The SMAP L4 product provides soil moisture measurements at a 9 km spatial resolution and 3-hour temporal resolution. The detailed description of SMAP Level-4 can be found in the SMAP Handbook (<https://smap.jpl.nasa.gov/data/>).

Besides, as the successor of ERA-Interim, the ERA5-Land (ERA-5) reanalysis product is the latest generation of global reanalysis data developed by the European Centre for Medium-Range Weather Forecasts (ECMWF) using the 4D-Var data assimilation technique (Hersbach et al., 2020). In this study, ERA-5 Land hourly data collected from Climate Data Store (CDS) with a 0.1° spatial resolution was adopted. A total of three variables was selected including skin temperature (i.e., land surface

temperature), volumetric soil water layer 1 (0-7 cm) and total precipitation. The measurements at 9:00 am (UTC) were selected, which was close to the MODIS overpass time in the HOAL catchment.

2.2.3 In-situ Soil Moisture Measurement

Presently, ISMN is one of the most commonly used platforms to collect and publish globally distributed in-situ soil moisture data (Dorigo et al., 2021). In this study, the HOAL network, a densely distributed soil moisture network from ISMN, was introduced as the primary source of in-situ soil moisture measurements. The sensors in the HOAL network provide hourly soil moisture and soil temperature data at depths of 5, 10, 20, and 50 cm. In this study, the in-situ soil moisture measurements from a total of 24 in-situ sensors from April to October in 2017 and 2018 were used. Since this study focused on surface soil moisture, only 0-5 cm soil moisture measurements were selected, which was consistent with the SMAP SSM product. Based on the data quality flags provided by ISMN, only data flagged by "G" (good quality) was included while the missing and low-quality values were not considered in this study. In addition, we also collected other auxiliary in-situ measurements from HOAL catchment including soil texture (i.e., clay, silt, and sand contents), observed precipitation, and crop management.

3. Methods

3.1 Methodology

The proposed framework of Generating high Resolution, Accurate, Seamless data using Point-Surface fusion (GRASPS) is illustrated in Fig. 2. There are four steps to generate 3H SSM data: (1) Data collection and preprocessing (Section 3.2); (2) Generation of 30 m seamless LST and surface reflectance (Section 3.3); (3) Deep learning based SSM downscaling (Section 3.4); (4) Pixel classification based bias correction (Section 3.5). More detailed descriptions are outlined below.

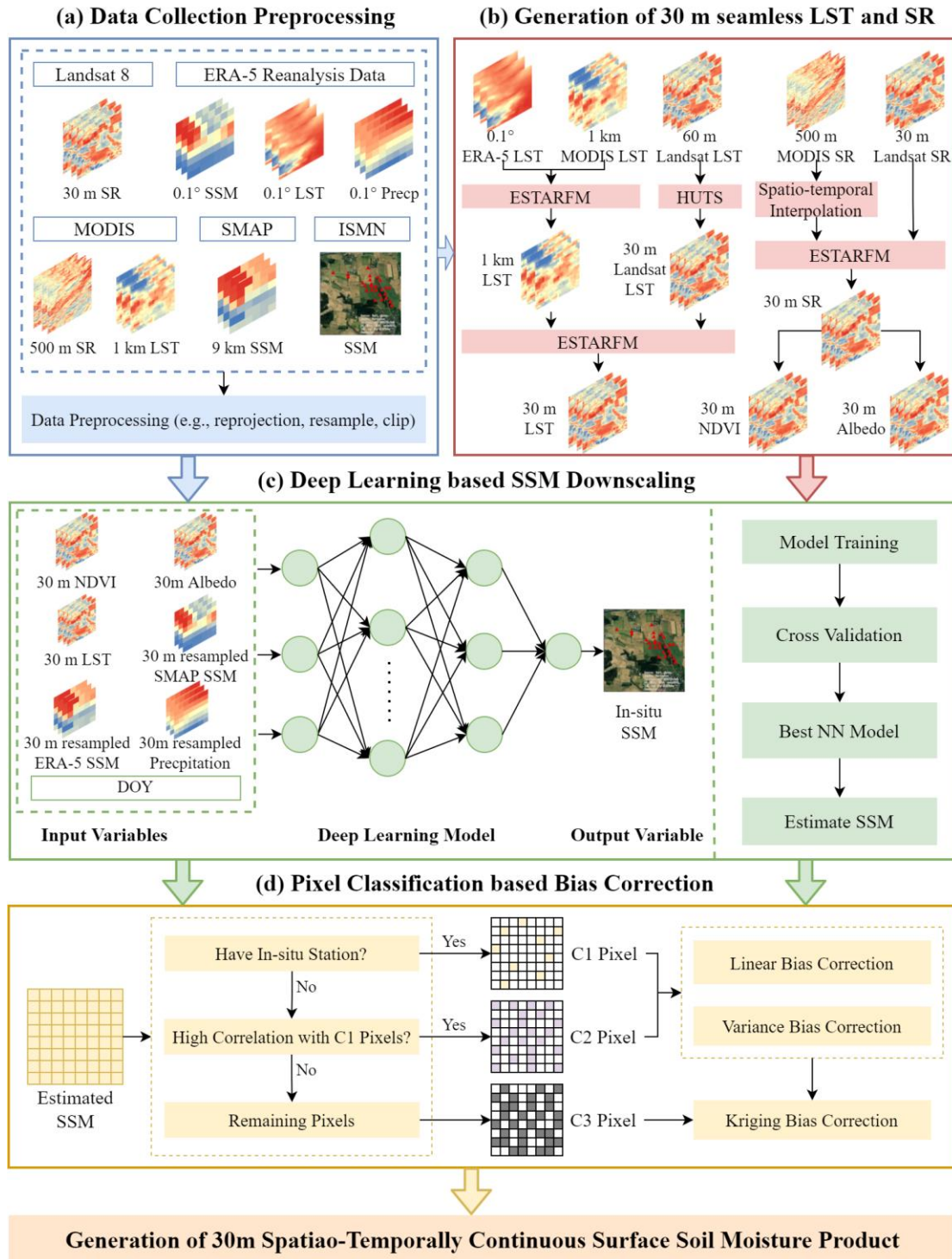


Fig. 2. The proposed SSM fusion Methodology (GRASPS). Four steps of the method: (a) Data collection and preprocessing; (b) Generation of 30 m seamless LST and surface reflectance; (c) Deep learning based SSM downscaling; (d) Pixel classification based bias correction.

3.2 Data collection and preprocessing

The GRASPS framework integrated multi-source data sets including remotely sensed products, model-based products, and ground measurements. To ensure the consistency of the spatial extent and make the products comparable, all products were reprojected to UTM projection with WGS84 datum by ArcGIS software, and all images were clipped based on the boundary of the study area. Since our study focused on the generation of 30 m SSM data, some SSM related variables (i.e., precipitation, SMAP SSM, and ERA-5 SSM) were resampled to 30 m by a bilinear interpolation algorithm.

3.3 Generation of 30 m seamless LST and surface reflectance

This study applied ESTARFM to fuse multiple land surface variables and generate 30 m spatio-temporally continuous inputs (i.e., NDVI, LST, Albedo) for the subsequent SSM fusion model. ESTARFM considers the temporal trend of the reflectance variation and combines the spatial and spectral similarity to reconstruct each central pixel in the search window. Compared to STARFM, ESTARFM improves the fusion accuracy in regions with strong heterogeneity in land cover.

The inputs of ESTARFM include two pairs of high-resolution images (HRI) and low-resolution images (LRI) at two calculation dates and one LRI at the prediction date. The implementation of ESTARFM can be divided into three parts. First, both HRIs and LRIs at calculation dates are reprojected and clipped to match the extent of the study area, while LRIs are resampled to be consistent with spatial resolution of HRIs using a bilinear resampling algorithm. Second, for each central pixel, pixels with similar spectral features within a predefined search window (window size is equal to 51 pixels in this study) are extracted and used to calculate corresponding weights and conversion coefficients. Here the neighboring pixels with similar spectral characteristics as the central pixel in the search window are defined as "similar" pixels, which are searched using an unsupervised clustering algorithm. Finally, based on the weights and conversion coefficients, the LRI at the prediction date is reconstructed to a high spatial resolution (equal to the resolution of HRI). The core equations of ESTARFM are given as follows:

$$F_k(x_{w/2}, y_{w/2}, t_p, B) = H(x_{w/2}, y_{w/2}, t_k, B) + \sum_{i=1}^N W_i \times V_i \times (L(x_i, y_i, t_p, B) - L(x_i, y_i, t_k, B)) \quad (1)$$

$$F(x_{w/2}, y_{w/2}, t_p, B) = T_m \times F_m(x_{w/2}, y_{w/2}, t_p, B) + T_n \times F_n(x_{w/2}, y_{w/2}, t_p, B) \quad (2)$$

where $(x_{w/2}, y_{w/2})$ is the central pixel in the search window of size w . $t_k (k = m, n)$ indicates the calculation dates while t_p means the prediction date. N is the number of similar pixels while W_i and V_i represent the weight and conversion coefficient for similar pixel i , respectively. B means the bands. H and L denote high-resolution images and coarse resolution images, respectively, while F is the predicted high-resolution image. Since there are two predicted images at t_m and t_n , the final predicted fine image is their weighted sum. The weight at T_k is calculated as:

$$T_k = \frac{1 / \left| \sum_{j=1}^w \sum_{i=1}^w L(x_i, y_j, t_k, B) - \sum_{j=1}^w \sum_{i=1}^w L(x_i, y_j, t_p, B) \right|}{\sum_{k=m,n} (1 / \left| \sum_{j=1}^w \sum_{i=1}^w L(x_i, y_j, t_k, B) - \sum_{j=1}^w \sum_{i=1}^w L(x_i, y_j, t_p, B) \right|)} \quad (3)$$

More details about the ESTARFM procedure and calculation can be found in Zhu et al. (2010). Here MODIS LST and MODIS surface reflectance were chosen to perform the ESTARFM algorithm. Taking LST as an example, since MODIS LST during the study period had missing or low quality values due to cloud cover, the ERA-5 LST and clear-sky MODIS LST were firstly used to generate $1 \text{ km} \times 1 \text{ km}$ continuous LST by ESTARFM. Then the 1 km spatio-temporally continuous LST and 30 m clear-sky Landsat LST were input into ESTARFM again to generate 30 m spatio-temporally continuous ESTARFM LST.

Similarly, considering the cloud effects, missing and outlier values in the 500 m MODIS surface reflectance product were excluded firstly based on the quality control information. The gaps of MODIS images were further filled based on a spatial and temporal reconstruction algorithm (Yang et al., 2018). Afterwards, the gap-filled 500 m MODIS surface reflectance was fused with 30 m clear-sky Landsat surface reflectance using ESTARFM to produce 30 m continuous reflectance data. Finally, 30 m ESTARFM NDVI and ESTARFM Albedo were calculated following the equations

below:

$$NDVI = (B_4 - B_3) / (B_4 + B_3) \quad (4)$$

$$Albedo = 0.365 * B_1 + 0.13 * B_2 + 0.373 * B_3 + 0.085 * B_4 + 0.072 * B_5 - 0.0018 \quad (5)$$

where $B_1 - B_5$ are the reflectance values of blue, green, red, NIR, and SWIR bands, respectively.

3.4 Deep learning based SSM downscaling

Deep belief network (DBN), a Bayesian probability generation model, has shown excellent performance in data fusion (Shen et al., 2020; Wu et al., 2020; Li et al., 2017; Yang et al., 2017; Hinton et al., 2006). In this study, DBN was used for an attempt to downscale SSM. In addition to one input layer (for the input of multiple predictors) and one output layer (for the output of in-situ SSM), the traditional DBN is composed of several restricted Boltzmann machines (RBM) layers and one back-propagation (BP) layer. The structure of classic DBN and RBM is shown in Fig. S1. Each RBM is a two-layer network, including one visible layer V and one hidden layer H . Neurons between two layers are fully connected while no connections exist between neurons in the same layer. The RBM is an energy-based probability model. Let v and h represent the state of the visible layer and the hidden layer. v_i and h_i mean the i th neuron of the visible and hidden layer, respectively. Then the energy function can be expressed as:

$$E(v, h / \theta) = -\sum_{i=1}^m a_i v_i - \sum_{j=1}^n b_j h_j - \sum_{i=1}^m \sum_{j=1}^n v_i W_{ij} h_j \quad (6)$$

where $\theta = \{W_{ij}, a_i, b_j\}$ is the parameter to be estimated. Specifically, W denotes the weight matrix while a and b represent the bias of the visible nodes and hidden nodes, respectively.

In this study, SSM was downscaled by fusing SSM background variables with remotely sensed, meteorological and temporal parameters, including SMAP SSM, ERA-5 SSM, ESTARFM LST, ESTARFM NDVI, ESTARFM Albedo, precipitation, and days of year (DOY). Correlation analysis between in-situ SSM and multiple

predictors was conducted and can be found in Supporting Information (SI) Text S1 and Fig. S2. Results revealed that in-situ SSM had a positive relationship with NDVI, precipitation, SMAP SSM, and ERA-5 SSM, whereas a negative relationship with LST, Albedo, and DOY. The downscaling model can be then expressed as follows:

$$SSM_{downscaled} = f(SMAP\ SSM, ERA-5\ SSM, ESTARFM\ LST, ESTARFM\ NDVI, ESTARFM\ Albedo, Precip, DOY) \quad (7)$$

where $f(\cdot)$ represents the DBN model. The training of DBN can be summarized in two steps: pre-training and fine-tuning. The pre-training step extracts significant features from the predictor variables, starting from the input layer to the hidden layer of the last RBM without supervision. At the end of the step, the parameters can be trained to be approximately close to the ideal values. In the fine-tuning step, the weights and biases are further refined to obtain more accurate predictions by the back-propagation algorithm.

In this study, the data from April to October in 2018 was used to train the DBN model, while data from April to October in 2017 was adopted to validate the downscaling performance. Considering that there were M sensors in the study area and the number of available in-situ SSM data for each sensor was N_i ($i = 1 \dots M$) in 2018, the 7 predictors then formed the input sample set of $S \times 7$ (here $S = \sum_{i=1}^M N_i$, which was the number of total samples) while the shape of the output (i.e., in-situ SSM) set was $S \times 1$ ($S = \sum_{i=1}^M N_i$). Then the training sample set was input into the DBN model. Cross-validation was implemented to evaluate the performance of the models. Based on the best-fitted DBN model, the data in 2017 at the in-situ sensors was used to validate the downscaling accuracy. Five statistical metrics were adopted to evaluate the downscaling performance, including Pearson correlation coefficient (PCC), root mean square error (RMSE), bias, unbiased root mean square error (ubRMSE) and mean absolute error (MAE). The equation, unit, and range for each metric are listed in Table S1. Meanwhile, the downscaling performance of the DBN model was also compared with the other two widely used statistical downscaling algorithms including back-propagation neural network (BPNN) and random forest (RF). The detail information of these two methods can refer to Rumeihart and Hinton (1986) and Breiman (2001).

Finally, from April to October in 2017, SSM related variables at each pixel in the study were obtained following Section 3.2 and 3.3. And the best DBN model was applied to produce spatio-temporally continuous daily SSM at $30\text{ m} \times 30\text{ m}$ spatial resolution for the entire study region.

3.5 Pixel Classification based Bias Correction

Although the steps mentioned above were able to generate $30\text{ m} \times 30\text{ m}$ spatio-temporally continuous downscaled SSM, the downscaled SSM may still contain biases, relative to in-situ observations. The deviation may be attributed to the error propagation from the downscaled SSM auxiliary variables (e.g., NDVI, Albedo, LST) and other background fields (e.g., SMAP SSM, ERA-5 SSM, precipitation) when resampling from coarse resolution to high resolution (i.e., 30 m). In order to further improve the accuracy and minimize the systematic biases of downscaled SSM, we proposed a pixel classification based bias correction method. The bias correction method here follows the assumptions below (Brocca et al., 2010; Cosh et al., 2004; Heathman et al., 2012):

- 1) The in-situ SSM measurements are the most reliable and accurate values for reference purposes and the spatial representativeness error of in-situ sensors is small at the $30 \times 30\text{ m}$ scale.
- 2) In every $30\text{ m} \times 30\text{ m}$ pixel, the actual soil moisture value is homogeneous because of its relatively small coverage (compared to $1\text{ km} \times 1\text{ km}$ or larger; Crow et al., 2012).
- 3) Every in-situ ground sensor can measure the soil moisture value around itself because all sensors are strictly quality controlled at the location.

The pixel classification-based correction process is designed according to the following three steps:

- 1) Pixel classification. All pixels in the study area were classified into one of the three types: C1 (pixels containing one or more in-situ SSM sensors with sufficient amount of data), C2 (pixels environmentally and statistically similar to C1), C3 (pixels that do not belong to either C1 or C2).

- 2) Formulation of bias correction strategies for different types of pixels. The details of each rule are given below.
- 3) Bias correction for each type of pixel based on the corresponding rule to improve the accuracy of downscaled SSM.

3.5.1 Rule 1 for C1 Bias Correction

For C1 pixels, the ground measurements (which were treated as true values) were used to correct the bias for the downscaled SSM. First, the linear scaling approach was performed between in-situ and downscaled SSM for each C1 pixel (Leander and Buishand, 2007). The equations of linear correction are given as follows:

$$Bias = \mu(SSM_{down}^{origin}) - \mu(SSM_{ground}) \quad (8)$$

$$SSM_{down}^{s1} = SSM_{down}^{origin} - Bias \quad (9)$$

where SSM_{down}^{origin} and SSM_{ground} are the originally downscaled SSM and in-situ SSM, respectively. SSM_{down}^{s1} is the SSM after linear correction ($s1$ indicates step 1). μ represents the average value of the SSM series. To be more consistent with the ground measurements, the variance scaling approach was also carried out (Chen et al., 2011):

$$SSM_{down}^{s2} = SSM_{down}^{s1} - \mu(SSM_{down}^{s1}) \quad (10)$$

$$Ratio = \sigma(SSM_{ground}) / \sigma(SSM_{down}^{s2}) \quad (11)$$

$$SSM_{C1} = \mu(SSM_{down}^{s1}) + SSM_{down}^{s2} \times Ratio \quad (12)$$

where SSM_{C1} indicates the corrected SSM for C1 pixels. SSM_{down}^{s2} is the deviation between SSM_{down}^{s1} and its mean value ($s2$ indicates step 2), σ means variance.

By implementing the linear and variance scaling approach, the originally downscaled SSM at C1 pixels would have the same mean and standard deviation as the in-situ SSM. In the process of Rule 1, the pixels with sensors that have sufficient amount of in-situ SSM data were treated as C1 pixels. The remaining pixels with in-situ sensors were then considered as the test sites for the validation of C2 and C3

correction.

3.5.2 Rule 2 for C2 Bias Correction

It is reasonable to assume that statistically and environmentally similar patterns exist in SSM time series between one certain pixel (C2) and C1 pixels. Here statistical similarity indicates that each SSM variable (i.e., downscaled SSM, SMAP SSM, ERA-5 SSM) has a strong relationship (i.e., PCC values) between two pixels while the environmental similarity means that each environmental variable (i.e., LST, NDVI, precipitation) has high PCC value between two pixels. To this point, it is feasible to correct the C2 pixels by utilizing the appropriate correction technique at corresponding C1 pixels with a significantly statistical and environmental relationship. In this study, a highly statistical and environmental similarity is defined as:

$$\begin{aligned} & |PCC_{downscale}| > 0.7 \cap |PCC_{NDVI}| > 0.7 \cap |PCC_{Albedo}| > 0.7 \cap |PCC_{LST}| > 0.7 \cap \\ & |PCC_{Precip}| > 0.7 \cap |PCC_{ERA5\ SSM}| > 0.7 \cap |PCC_{SMAP\ SSM}| > 0.7 \end{aligned} \quad (13)$$

where PCC represents the Pearson correlation coefficient between the time series of two pixels. Except for C1 pixels, each pixel in the study area was considered as a potential C2 pixel. Only pixels satisfying this criterion could be finally regarded as C2 pixels. In this study, the threshold (PCC value) was tested from 0.5 to 0.9 with an interval of 0.1. Finally, the threshold was set as 0.7 by trial and error, which showed the highest downscaling accuracy over the validation sites. More detailed information about the selection of this threshold can be found in SI Text S2 and Fig. S3.

After the identification of C2 pixels and their corresponding C1 pixels, the bias correction of C2 can be defined as:

$$SSM_{down,i}^{s1} = SSM_{down}^{origin} - Bias_i \quad (i = 1, 2, \dots, N) \quad (14)$$

$$SSM_{C2} = \frac{1}{N} \sum_{i=1}^N (\mu(SSM_{down,i}^{s1}) + Ratio_i * (SSM_{down,i}^{s1} - \mu(SSM_{down,i}^{s1}))) \quad (15)$$

where SSM_{down}^{origin} is the originally downscaled SSM of a specific C2 pixel. i is the i th statistically similar C1 pixel. N represents the number of C1 pixels highly correlated with a C2 pixel. $Bias_i$ and $Ratio_i$ mean the linear and variance scaling

factors of the i th C1 pixel. SSM_{C2} represents the finally corrected SSM for a C2 pixel.

3.5.3 Rule 3 for C3 Bias Correction

The remaining pixels other than C1 and C2 pixels are classified as C3 pixels. The identification of C1 and C2 pixels provides reference data for the bias correction of C3 pixels. Thus, we used a Kriging-based bias compensation method to correct C3. Specifically, we first calculated the bias between the SSM series before and after the bias correction for C1 and C2 pixels, which is given as follows:

$$Bias(x, y, t) = SSM_{correct}(x, y, t) - SSM_{down}(x, y, t) \quad (16)$$

where (x, y, t) represents the location of a pixel at a specific time. Then, the Kriging interpolation algorithm was adopted to interpolate the biases to the entire study region for each day during the study period. Finally, the corrected SSM at C3 pixels can be defined as:

$$SSM_{C3} = SSM_{down}^{origin} + Bias_{Kriging} \quad (17)$$

In this study, there are a total of 24 pixels with sensors. Among them, 12 pixels were flagged by C1. The remaining 12 pixels were selected for validation of the bias correction method. Specifically, six of them which were statistically and environmentally similar with C1 pixels were regarded as C2 validation pixels while the other six pixels were considered as C3 validation pixels. After the application of these three rules for bias correction, we finally generated 30 m \times 30 m 3H SSM.

4. Results

4.1 Performance of the Ancillary Variables Downscaling

In order to provide high-quality inputs for the deep learning-based GRASPS model, we fused MODIS and Landsat datasets (i.e., surface reflectance and LST) using the ESTARFM algorithm to generate 30 m \times 30 m spatio-temporally continuous land

surface variables. Landsat data was used for validation because the ground truth was merely unknown and other data sets had their own biases and errors. The accuracy and spatial patterns of NDVI, Albedo, and LST obtained from MODIS, Landsat, and ESTARFM fusion for the whole study area (Fig. 3) at the validation date of 20 May (which were not used in ESTARFM) were provided.

Compared to the coarse and obscure NDVI distribution derived from MODIS reflectance, we found that NDVI downscaled by ESTARFM were more spatially detailed with fewer mosaic effects. The downscaled NDVI showed high consistency with Landsat NDVI (regarded as true value) for PCC, RMSE, and bias achieving 0.93, 0.091 and -0.034, respectively. The densely distributed (red) scatter points were mostly concentrated around the diagonal in Fig. 3f. Similarly, PCC, RMSE, and bias between downscaled Albedo and Landsat Albedo reached 0.94, 0.01, and -0.003, respectively. Downscaled LST also had PCC, RMSE, and bias at 0.91, 1.38 K, and 0.74 K, despite an overall positive deviation from the diagonal (Fig. 3r). The spatial distribution of downscaled variables was highly consistent with that of Landsat retrieved images. The areas with high LST and low NDVI values were generally in accordance with the built regions and farmland. Based on these results, it was clear that the ESTARFM algorithm exhibited excellent performance in generating $30\text{ m} \times 30\text{ m}$ spatio-temporally continuous Landsat-like surface variables.

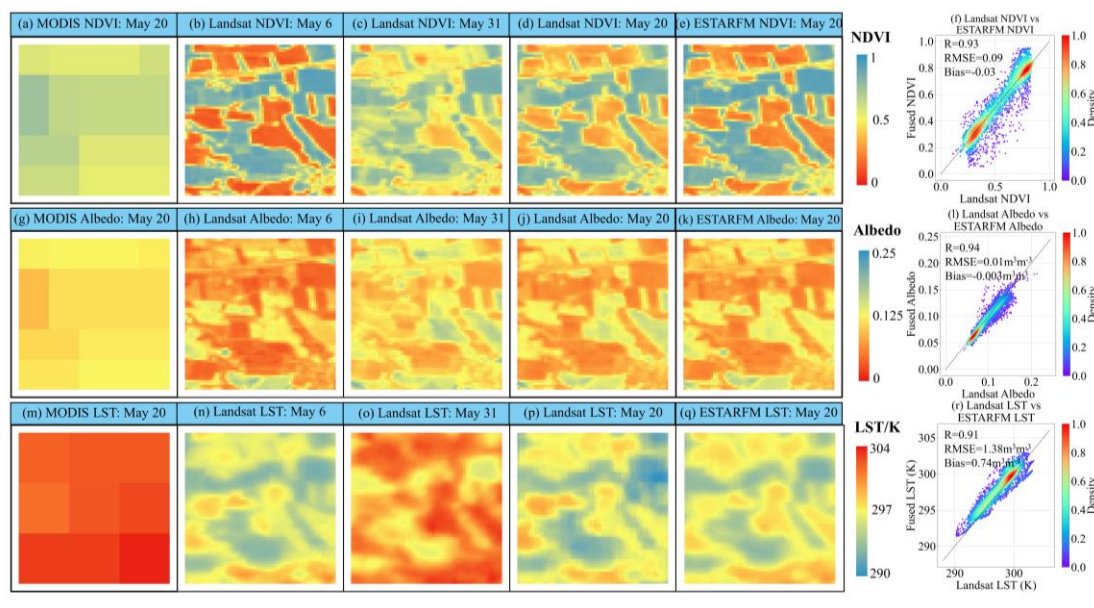


Fig. 3. The spatial distributions and validations of the downscaled NDVI, LST, and Albedo on May 20, 2018. The dates of Landsat data input in the ESTARFM were May 6, 2018 and May 31, 2018. The first to the third row indicate NDVI, Albedo, and LST, respectively. The first column shows the original MODIS image for each variable while the second and the third columns represent input Landsat images at prediction dates, respectively. The fourth column indicates the Landsat images at the calculation date (20 May, 2018). The fifth column lists the 30 m spatio-temporally continuous downscaled NDVI, Albedo, and LST provided by the ESTARFM model. Here the unit of LST is Kelvin (K). The last column represents the scatter density plots of the downscaled variables against Landsat retrieved variables. The redder the color, the denser the distribution of the scatter points.

4.2 Evaluation of the Downscaled SSM

4.2.1 Overall Performance at Validation Sites

By integrating high-quality downscaled surface variables (Section 4.1) and other background fields, the DBN model was built using data from April to October 2018. In-situ SSM in 2017 were used to evaluate the performance of the downscaled SSM. The scatter plots of the downscaled SSM (red points) against in-situ measurements for 16 randomly selected validation sites are shown in Fig. 4. Meanwhile, the corresponding SMAP SSM (blue points) and ERA-5 SSM (green points) were added for comparative analysis.

Validation results showed that the PCC, RMSE, and bias of the downscaled SSM against in-situ SSM ranged from 0.56-0.96, 0.019-0.076 m^3m^{-3} , and -0.056-0.050 m^3m^{-3} , respectively (Fig. 4). The scatter points were distributed close to the 1:1 line, indicating the DBN-based fusion method had potential to produce 3H SSM data. As shown in Table S2, the average accuracy of downscaled SSM (with average of PCC and RMSE of 0.81 and 0.042 m^3m^{-3}) and SMAP SSM (with average of PCC and RMSE of 0.72 and 0.046 m^3m^{-3}) was higher than ERA-5 SSM (with average of PCC and RMSE of 0.67 and 0.066 m^3m^{-3}). The results demonstrated that the overall

performance of downscaled SSM was better than SMAP SSM, although SMAP SSM could also fit relatively well with the in-situ SSM. It is possible that the observed SSM of a site can approach the general SSM temporal variation of the study region, which can be further in line with the areal SSM product (i.e., SMAP and ERA-5 SSM). However, the satellite/model-based SSM with a coarse spatial resolution (i.e., 9 km and 0.1°) would fail to represent detailed spatial information of the actual SSM distribution at field scale (i.e., 30 m). In addition, the correlation analysis also indicated the difference between SMAP SSM and ERA-5 SSM (with PCC of 0.73). To this point, the accuracy of SMAP SSM and ERA-5 SSM could vary in different in-situ sites.

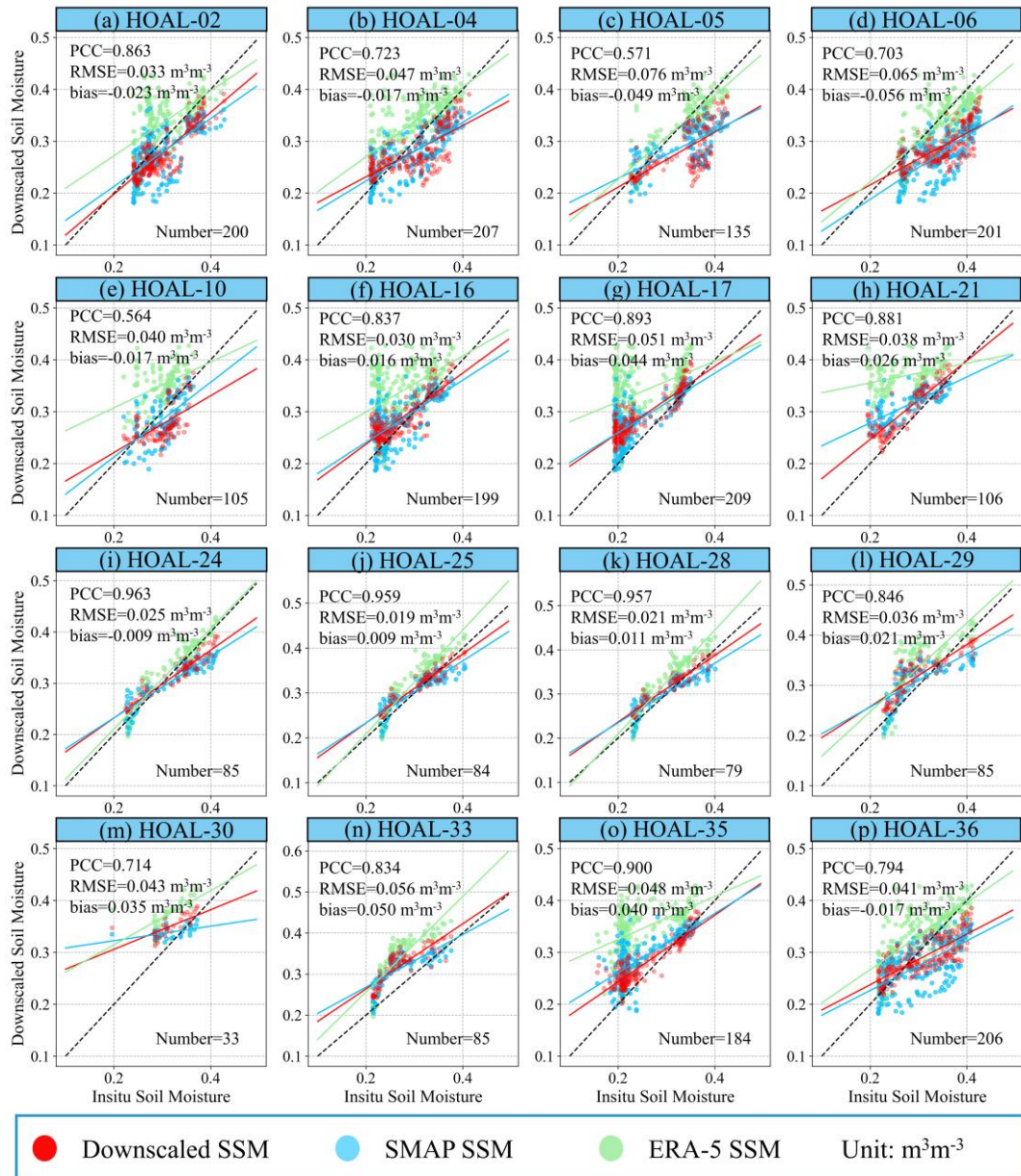


Fig. 4. The scatter plots and statistical metrics (PCC, RMSE, bias) of the downscaled SSM, original ERA-5 SSM, and SMAP SSM against in-situ SSM. Red, blue, and green points represent downscaled SSM, SMAP SSM, and ERA-5 SSM, respectively. "Number" indicates the number of sample sizes for each in-situ sensor. The unit of SSM is m^3m^{-3} .

Moreover, we evaluated the spatial variation of the model performances, and the spatial distribution for each statistical metric is shown in Fig. 5. We found that the sensors located in the central part of the HOAL catchment showed higher correlation coefficients and stronger relationships than the northwest region with few in-situ sensors. The distributions of RMSE, ubRMSE, and MAE showed similar patterns as PCC. Fig. 5f shows the statistics of all evaluation metrics. Based on the deep learning downscale model, the downscaled SSM exhibited an average PCC, RMSE, bias, ubRMSE, and MAE of 0.78, $0.048 m^3m^{-3}$, $-0.001 m^3m^{-3}$, $0.033 m^3m^{-3}$, and $0.041 m^3m^{-3}$ over all validation sites. In addition, we further investigated the effects of site locations and land cover on the SSM downscaling performance. Specifically, the in-situ sites were grouped as hillslope (HS) sites and valley bottom (VB) sites (i.e., near weather stations or wetland areas close to the riparian forest), while the land cover types were classified into two groups including CROP (i.e., within agricultural field) and NO-CROP (i.e., positioned in forest and grassland sites, as well as at the edges of agricultural fields). The classification for all validation sites are shown in Fig. S4. The values of statistical metrics for these cases are shown in Table S3. The results demonstrated that the downscaling accuracy in HS locations (with average PCC, RMSE, ubRMSE, MAE of 0.78, $0.046 m^3m^{-3}$, $0.032 m^3m^{-3}$, $0.038 m^3m^{-3}$) was significantly higher than in VB locations (with average PCC, RMSE, ubRMSE, MAE of 0.75, $0.052 m^3m^{-3}$, $0.034 m^3m^{-3}$, $0.044 m^3m^{-3}$). In general, the SSM was more humid in VB sites due to the abundant vegetation cover, ponding around weather station, and wetland areas. However, previous studies have confirmed that the downscaling performance was usually poorer in humid conditions due to the weaker link between soil moisture and evapotranspiration, which was consistent with the statistical results in this study (Song et al., 2021; Zhang et al., 2016; Malbêteau et al., 2016).

Besides, previous studies showed that the growth of crops and crop structure (e.g., crop height) may complicate the performance of SSM downscaling (Gómez-Plaza et al., 2001). Therefore, we evaluated the impacts of land cover on the accuracy of downscaled SSM. Results demonstrated that NO-CROP locations (with average PCC, ubRMSE, and MAE of 0.818, 0.030 m^3m^{-3} , and 0.039 m^3m^{-3} , respectively) showed higher accuracy than CROP sites (with average PCC, ubRMSE, and MAE of 0.730, 0.034 m^3m^{-3} , and 0.042 m^3m^{-3} , respectively), which was consistent with the finding from Zappa et al. (2019). The differences in the downscaling accuracy between different vegetation types (i.e., CROP and NO-CROP) can be expected because the vegetation types, as well as the phenological stages, can substantially affect the local environmental conditions. Besides, various canopy properties (e.g., fractional vegetation cover and vertical structure) can influence the evapotranspiration, interception, percolation, and satellite observations. Gomez-Plaza et al. (2001) concluded that the controls regulating SSM spatial patterns were distinct in vegetated and non-vegetated regions, while Hupet and Vanclooster (2002) also found the considerable roles of vegetation in affecting spatial organization of soil moisture, which were consistent with the findings in our study.

We also conducted comparative experiments by introducing the other two widely used downscaling algorithms which were BPNN and RF. Downscaling results on all validation sites confirmed the effectiveness of DBN model in generating high accuracy downscaled SSM. More details about the comparative analysis can be found in SI Text S3. The statistical results and analysis above demonstrated that GRASPS framework represented great potential in generating field-scale SSM, maintaining high consistency with in-situ SSM.

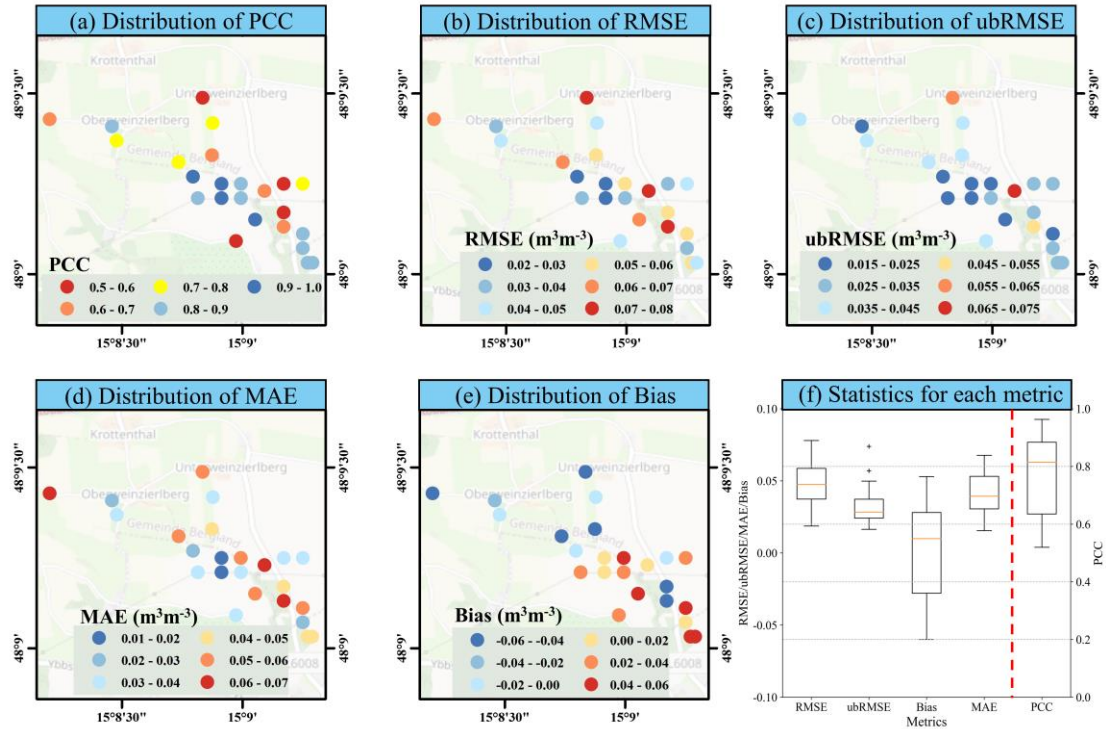


Fig. 5. Spatial variations and overall statistics of the evaluation metrics. (a)-(e) show the spatial distribution of PCC, RMSE, ubRMSE, MAE, and bias for the downscaled SSM against in-situ SSM measurements. The units for RMSE, ubRMSE, MAE, and bias are m^3m^{-3} . The last boxplot shows the statistical distributions of each metric.

4.2.2 Temporal Variation of the Downscaled SSM

We further evaluated our framework based on two additional criteria. The first is the capacity of SSM in capturing the temporal dynamics of ground soil moisture measurements. The second is the reliability of downscaled SSM in reconstructing the actual soil moisture distribution in the study area. To discuss whether the downscaled SSM estimated by the DBN model in GRASPS meets the temporal variation criterion, the performance of temporal variability of the downscaled SSM and original SSM background fields against in-situ SSM measurements were evaluated. A total of three in-situ SSM stations located at the west, central, and east of the study area with relatively complete data recording were selected to visualize their temporal variations of SSM. The SSM time series of each SSM product from April to October in 2017 along with precipitation events are illustrated in Fig. 6.

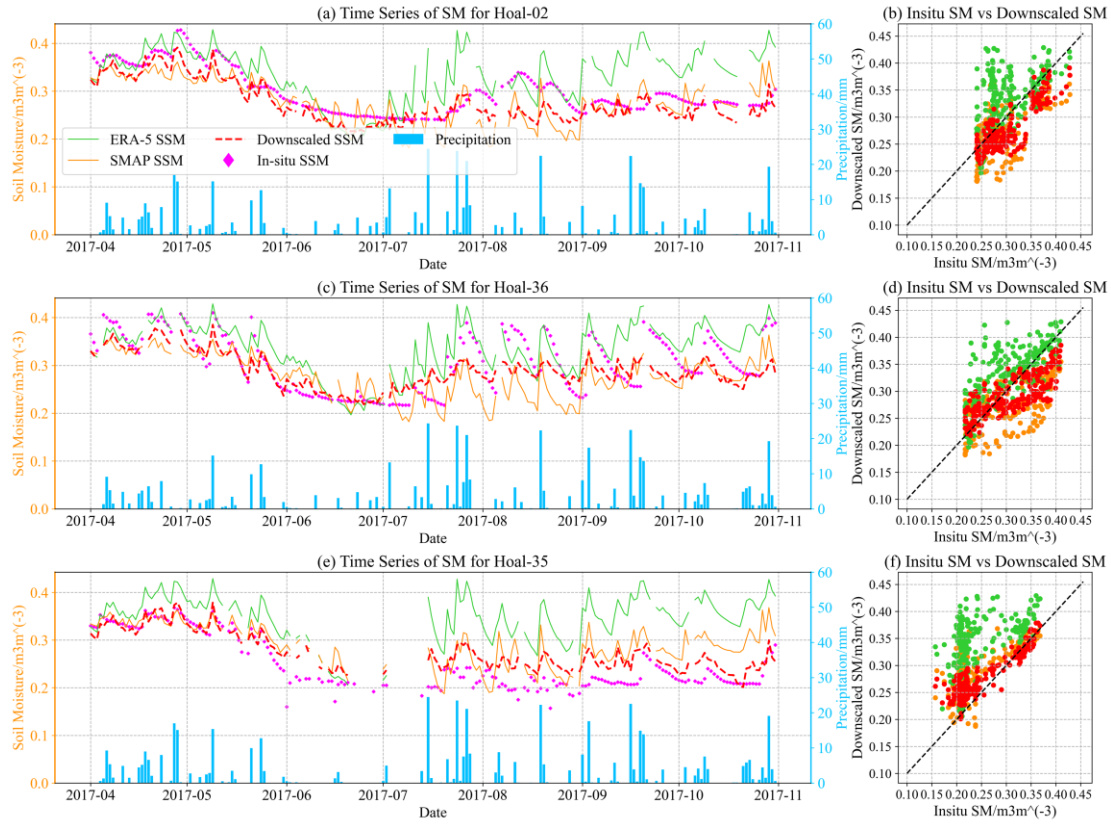


Fig. 6. Temporal variations of downscaled SSM, in-situ SSM, ERA-5 SSM and SMAP SSM at three validation sites. The purple points show the in-situ SSM records while the red dotted line represents downscaled SSM. Orange and green lines indicate SMAP SSM and ERA-5 SSM, respectively. The blue bar chart on the bottom denotes the rainfall events. The units for SSM and precipitation are m^3m^{-3} and mm, respectively. The right column lists the scatter plots of each SSM data set against in-situ SSM. The colors correspond to the data in the left column.

In general, the SSM at these three validation sites experienced a downward trend and an upward trend from April to October in 2017. The SSM values in HOAL-02 ($0.30 m^3m^{-3}$ in average) and HOAL-36 ($0.31 m^3m^{-3}$ in average) were relatively higher than that in HOAL-35 ($0.25 m^3m^{-3}$ in average), which may be partially related to the higher clay content (i.e., retaining more water) and lower sand content in HOAL-02 (21.4% and 6.5%) and HOAL-36 (20.6% and 7.2%) than HOAL-35 (18.1% and 8.9%). Relatively higher SSM values mainly occurred in April, July, and September with an average rainfall amount of 3.3 mm/day, 4.56 mm/day, and 3.08 mm/day, which

concentrated most rainfall events in the validation period. It can also be observed that the peak events of downscaled SSM and rainfall events fit well, especially during the summer. Besides, we also calculated the average NDVI value for each month in these validation sites. Results indicated that NDVI showed an increasing trend from April to July (increased from 0.51 to 0.69), of which the period was the major growth period of winter wheat and winter barley in the catchment and matched well with the decrease of downscaled SSM. Then, the NDVI followed a downward trend from 0.69 to 0.27 from July to September when the winter wheat and barley were harvested. Previous studies have confirmed that the growth of crops would lead to the decrease of surface soil moisture, which was in line with the variations of SSM in this study (Leng et al., 2017). As shown in this result, SMAP SSM and downscaled SSM had a better similarity with the in-situ SSM than ERA-5 SSM. Although the increase and decrease of ERA-5 SSM were consistent with the variations of in-situ SSM, a significant overestimation was observed, particularly for the period from July to October. In comparison, SMAP SSM seemed to detect the temporal dynamics of in-situ SSM better than ERA-5 SSM, but a relatively large overestimation of SSM still existed from August to October. As mentioned above, this is mainly due to the fact that the role of spatial scale heterogeneity leading to differences between satellite retrieved SSM and in-situ measurements are often ignored. In other words, ERA-5 SSM and SMAP SSM had coarser spatial resolution (i.e., 0.1°, 9 km) than the field scale (i.e., 30 m) SSM. Therefore, the direct resampling from coarse resolution to 30 m would lose detailed spatial information, leading to the deviations with in-situ SSM. Particularly, the dynamic range (i.e., temporal variation) of SSM would be weakened when moving from a small scale to a larger scale (Abbaszadeh et al., 2018). But according to the statistical results for the validation shown in Fig. 4 and Fig. 6, the downscaled SSM was more approaching to (i.e., represented higher accuracy with) the in-situ SSM compared to the SMAP SSM and ERA-5 SSM.

Moreover, it can be seen that there were some periods when the temporal pattern of in-situ SSM differed from the downscaled and modeled SSM. For instance, from June to July in 2017, the in-situ SSM decreased while the downscaled SSM and

modeled SSM exhibited some peak events. To analyze the reason, we also used observed precipitation to downscale SSM instead of ERA-5 precipitation for comparison. The temporal variations of downscaled SSM at the three validation sites and the overall downscaling accuracy at all validation sites are shown in Fig. S6 and Fig. S7, respectively. In general, the temporal variations for the downscaled SSM using observed precipitation showed similar patterns with the SSM variations using ERA-5 precipitation. However, the periods when in-situ SSM showed different patterns with downscaled SSM still existed. Xaver et al. (2020) found that the SPADE sensors (set up in the HOAL catchment) represented weak or in some cases no reaction to the rainfall events. The weak response to the precipitation could be explained by the horizontally installation of the probes, which was less affected by the drying and wetting surface. Therefore, it can explain the different response of in-situ SSM and other SSM products during rainfall events. In addition, the downscaling model adopted SMAP SSM and ERA-5 SSM as input variables. The temporal dynamics of SMAP and ERA-5 products, as well as the ups and downs of precipitation values caused by the occurrence of rainfall events would be partly retained in the downscaled SSM based on the non-linear fitting mechanism of deep learning (Lin et al., 2022; Dong et al., 2021). To this point, the scale mismatch issue would also exert negative effects on the accuracy of downscaled SSM series through deep learning to a certain degree. Considering the analysis above, the downscaled SSM represented different temporal patterns compared to in-situ SSM at certain periods.

We also evaluated the monthly variations of the statistical metrics for the downscaled SSM as shown in Fig. 7. It can be observed that the general accuracy (based on PCC, RMSE, ubRMSE, bias, and MAE) of downscaled SSM was relatively higher from April to July compared to that from August to October. It may be associated with the limited capability of microwave remote sensing under the ripe summer crops (mainly maize in HOAL catchment), which further weakened the downscaling performance (Abowarda et al., 2021; Roman-Cascon et al., 2017;). During the later months, especially September, the errors of downscaled SSM against in-situ measurements were larger with PCC, RMSE, ubRMSE, bias, and MAE values of 0.22,

0.054 m^3m^{-3} , 0.028 m^3m^{-3} , 0.042 m^3m^{-3} , and 0.049 m^3m^{-3} , respectively. Zhang et al. (2016) concluded that the link between soil moisture variation and evapotranspiration processes is usually weaker in humid conditions than (semi-) arid conditions. The phenomenon can further weaken the SSM downscaling accuracy (Song et al., 2021). In dry condition, the SSM values is relatively low and thus result in higher evapotranspiration, which further lead to the enhancement of SSM feedbacks (Zhang and Dong, 2010; Li et al., 2018; Li et al., 2019). To this point, the lower SSM values in summer are generally easier to capture compared to less evaporative energy and more rain in autumn. As mentioned, about 8 soil moisture sensors were temporarily removed due to the local agricultural practices. Therefore, the insufficient number of training samples and changes of vegetation covers affected by the growing of summer crops may also lead to low accuracy in the later three months.

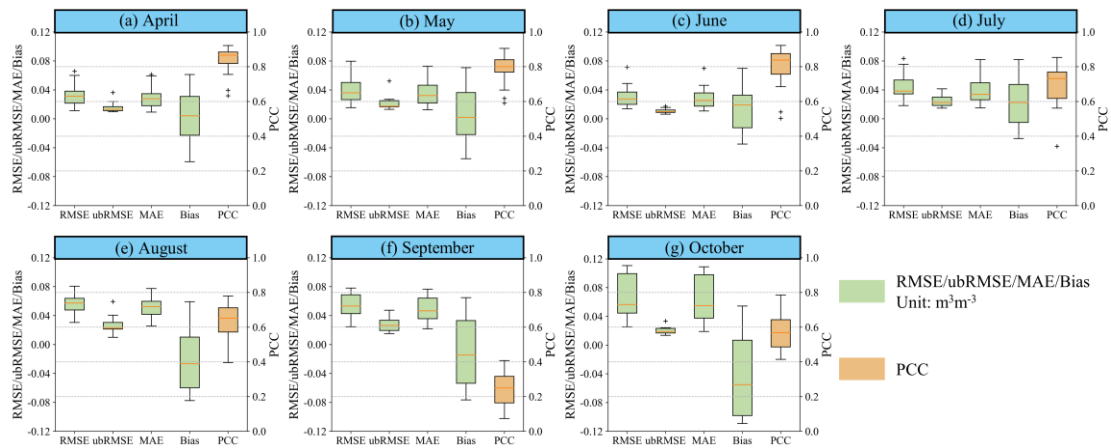


Fig. 7. Statistical metrics for the downscaled SSM from April to October. The y-axis of the PCC (orange) is shown on the right of the subplots. The unit for SSM is m^3m^{-3} .

4.2.3 Spatial Variation of the Downscaled SSM

Previous sections have discussed the performance of downscaled SSM against in-situ SSM measurements from a temporal perspective. The following is to present the performance of spatial distribution for the downscaled SSM. The spatial pattern of downscaled SSM is mainly dependent on the heterogeneity of input soil moisture related variables (e.g., NDVI, Albedo, LST), which showed substantial spatial variability in the study area (Abbaszadeh et al., 2018). The downscaled NDVI, Albedo,

LST and SSM at five consecutive days in May are presented in Fig. 8.

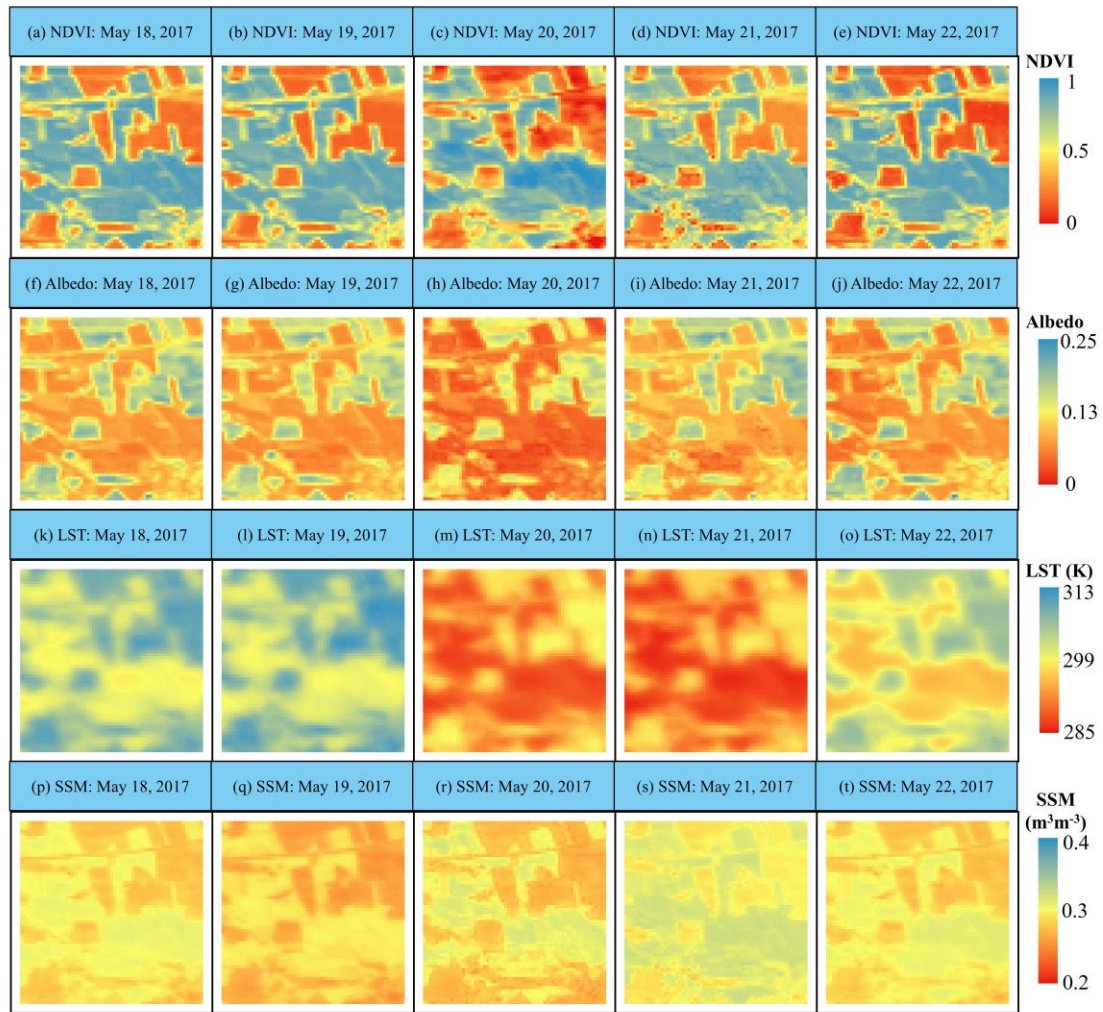


Fig. 8. Spatial distribution of the downscaled SSM and corresponding land surface variables (i.e., NDVI, Albedo, LST) at 5 consecutive days in May, 2017. The unit for SSM and LST are m^3m^{-3} and K, respectively.

Overall, the downscaled SSM in the study area ranged from $0.2 m^3m^{-3}$ to $0.4 m^3m^{-3}$ from May 18 to May 22. The detailed information of SSM spatial variation was well described based on the downscaled predictor variables. High consistency could be found between the downscaled SSM and other ESTARFM derived products. Specifically, relatively low downscaled SSM values usually corresponded to higher LST values. For instance, the northeastern and southwestern regions of the HOAL catchment showed higher LST than the other parts and thus had lower downscaled SSM, which was also consistent with the spatial patterns of the surface albedo. It was mainly

attributed to the fact that the surface albedo reflected the surface energy fluxes and the land cover, which had a close relationship with the capability of capturing the SSM spatial dynamics (Gascoin et al., 2009). In addition, days with relatively higher SSM values (e.g., May 20, May 21) also corresponded to those with relatively lower NDVI and LST values. This correlation was consistent with the relationship between soil moisture and the LST-NDVI trapezoidal feature space (Sabaghy et al., 2018; Tagesson et al., 2018; Zhu et al., 2017). Besides, days with relatively high SSM values were also consistent with the spatial distribution of precipitation occurrence. For instance, rainfall events occurred on May 20 (1.2 mm) and May 21 (11.9 mm), which led to the decrease of LST as well as the increase of SSM values. We also plotted the spatial distribution of downscaled SSM from May 16, 2017 to June 14, 2017 (Fig. S8). Results confirmed the potential of the proposed GRASPS methodology to produce $30\text{ m} \times 30\text{ m}$ spatio-temporally continuous SSM by using point-surface data fusion and a deep learning model. To further evaluate the effectiveness of the proposed framework in capturing SSM spatial dynamics, we quantitatively evaluated the spatial heterogeneity of the various SSM products (i.e., ERA-5 SSM, SMAP SSM, downscaled SSM, and in-situ SSM) in terms of the spatial standard deviation (SSD), which are shown in Fig. S9. In this study, we only calculated the SSD at a given time when at least 10 data samples were available simultaneously. It can be seen that the SSD of ERA-5 SSM and SMAP SSM showed low SSD values and insignificant SSD variations due to the huge differences between satellite footprint and the field scale. In comparison, although the in-situ SSM indicated higher SSD values, the downscaled SSM showed much better performance than the satellite/reanalysis SSM data, which further confirmed the capability of the deep learning based downscaling technique.

We also investigated the role of SSM background fields (i.e., SMAP SSM and ERA-5 SSM) and the ESTARFM technique in the generation of 3H SSM. The downscaling performances on validation sites using different input data combinations (Table S4) were compared. Results demonstrated that the inputs of both SMAP SSM and ERA-5 SSM could substantially improve the downscaling accuracy of the DBN model (Fig. S10). Besides, the spatial patterns for SSM in different scenarios also

confirmed that the application of ESTARFM technique could greatly improve the spatial details of the downscaled 3H SSM (Fig. S11). More descriptions about the exploration of input variables and ESTARFM technique can be found in SI Text S4.

4.3 Bias Correction of the Downscaled SSM

In order to further improve the overall accuracy of the downscaled SSM, we conducted the pixel classification-based bias correction method. To evaluate the performance of the bias correction algorithm, the downscaled SSM before and after the correction were validated at six C2 validation pixels and six validation C3 pixels. The comparison of the statistical metrics is shown in Fig. 9. Results demonstrated that RMSE, bias, and MAE for all validation sites decreased after the bias correction, although ubRMSE for two sites showed a slight increase. More specifically, RMSE, ubRMSE, bias, and MAE for corrected SSM ranged from 0.014-0.074 m^3m^{-3} , 0.013-0.054 m^3m^{-3} , -0.054-0.046 m^3m^{-3} , and 0.010-0.052 m^3m^{-3} , respectively. Overall, after correction, the average evaluation metrics (i.e., RMSE, ubRMSE, bias, and MAE) were lowered by 13%, 7%, 22%, and 18%, respectively. This accuracy improvement demonstrated the effectiveness of the bias correction method in GRASPS.

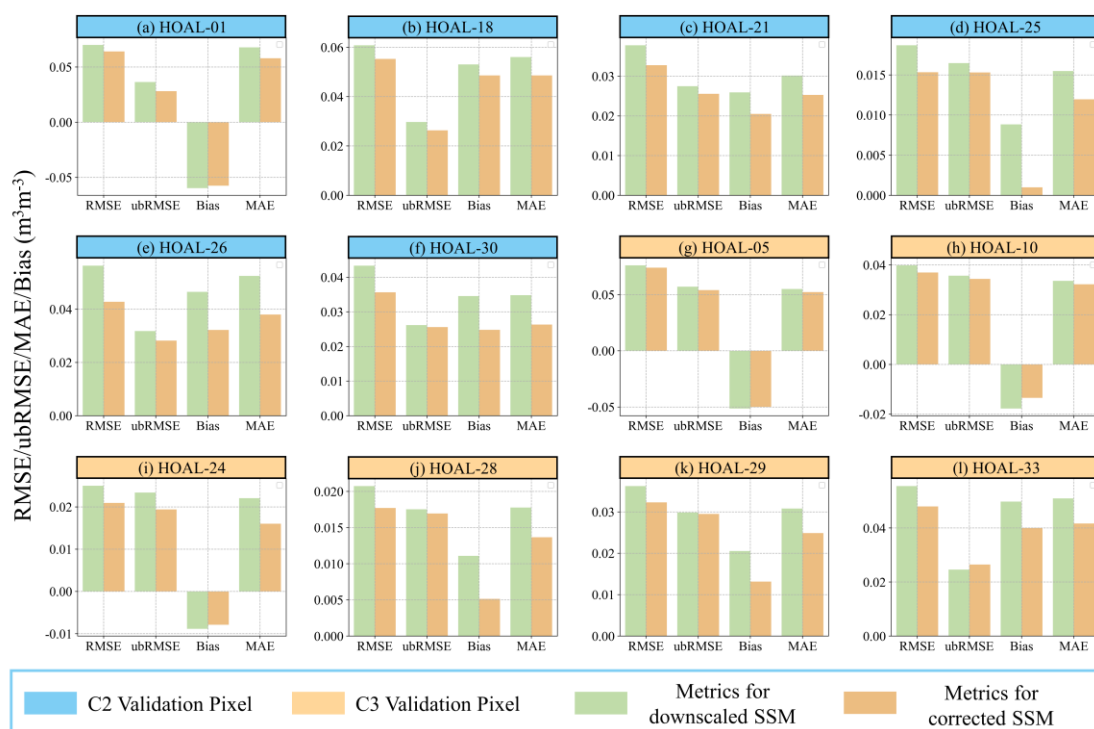


Fig. 9. The statistical metrics before and after the pixel classification based bias correction. The blue and orange subtitles represent validations for C2 and C3 pixels, respectively. For each subplot, the RMSE, ubRMSE, bias, and MAE before (green) and after (orange) bias correction are elaborated. The unit for each metric is m^3m^{-3} .

To further investigate the changes of SSM variations after bias correction, we plotted SSM time series for downscaled SSM, corrected SSM, and in-situ SSM for three C2 validation sites and three C3 validation sites (Fig. 10). Since the soil moisture measurements for C2 and C3 validation sites were not temporally continuous due to local agricultural practices, the SSM time series were not always continuous. It can be observed that corrected SSM series were relatively closer to the in-situ measurements. For the periods with large deviations between downscaled SSM and in-situ SSM, the downscaled SSM after bias adjustment tended to approach in-situ measurements more compared to the uncorrected downscaled SSM. Meanwhile, by averaging the correction information from multiple highly correlated C1 pixels, the high consistency between downscaled SSM and in-situ SSM could be partly retained (e.g., April to May at HOAL-21, HOAL-25, and HOAL-28).

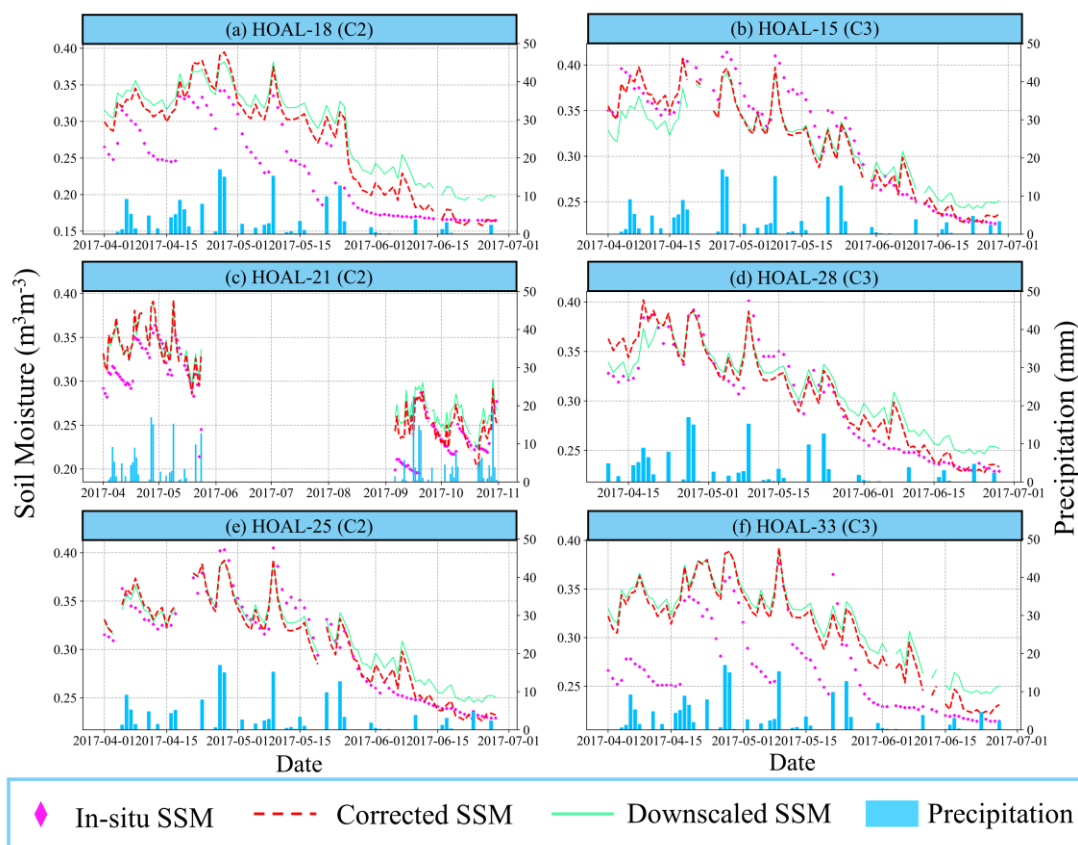


Fig. 10. Temporal variations of the downscaled SSM before and after bias correction against in-situ SSM. The purple points represent in-situ SSM while the red dotted line and green line indicate corrected SSM and downscaled SSM, respectively. The blue bar chart shows the rainfall events.

Finally, we compared the spatial patterns of downscaled SSM and corrected SSM at five consecutive days in June (Fig. S12). Generally, the corrected SSM resolved most spatial features of the original downscaled SSM distribution. The range of SSM in the catchment was changed from 0.18-0.30 m^3m^{-3} to 0.15-0.36 m^3m^{-3} . Some regions experienced decreasing SSM such as the southwestern region, the west-to-east road at the north of the study area, and locations surrounded by paved area in the figure. It may be due to the fact that the input SMAP SSM and ERA-5 SSM overestimated the SSM values compared to in-situ SSM, which further led to the overestimation of downscaled SSM. After correction, the overall distribution of SSM was more in line with the land cover pattern. For instance, the regions with drier soil moisture values generally corresponded to the agricultural areas. Besides, we also calculated the SSD for the

corrected SSM and the results are shown in Fig. S9. It can be seen that the overall SSD for the corrected SSM was higher than that for the originally downscaled SSM, which was more approaching to the SSD of in-situ SSM. This result demonstrated that after the bias correction, the spatial dynamics of the downscaled SSM had been better captured and maintained higher consistency with in-situ SSM.

Based on the aforementioned analysis and comparisons, the proposed SSM GRASPS method combining point-surface data fusion and deep learning achieved excellent performance in generating 3H (i.e., high resolution (30 m), high accuracy, and high spatio-temporal continuity (seamless and daily)) SSM.

5. Discussion

5.1 Comparison with previous researches

Existing studies initially explored how to generate soil moisture data with high resolution by fusing multiple remotely sensed, model-based, and in-situ data. Some methods were also developed such as spatial statistics, machine learning based regression, and multi-source data fusion (Jing et al., 2018). Table 2 lists several SSM fusion studies demonstrating the significant contribution of this study. Generally, most studies downscaled SSM using microwave remote sensing SSM and auxiliary data at the spatial resolution from 1 km to ~30 km. Such SSM products can be useful for large-scale studies, but are still insufficient for regional and field-scale water resources management, agriculture yield assessment, and numerical weather prediction. Moreover, due to the cloud contamination and deficiencies of available data, researchers seldom explored the generation of continuous SSM at field scale. Abbaszadeh et al. (2018) managed to generate 1 km SSM over the Continental United States (CONUS), but the missing and low-quality data in the remotely sensed LST product due to cloud contamination was not well filled. Zappa et al. (2019) also proposed a field-scale (30 m) SSM downscaling framework. However, relative to Zappa et al. (2019), our framework requires less in-situ observations and hence, can be easily applied to other study areas. Meanwhile, Abowarda et al. (2021) considered the

cloud effects on the auxiliary variables and generated 30 m SSM based on seven sites at Haihe Basin, China. In comparison, our study further addressed the uncertainty resulting from the heterogeneous distribution of SSM related variables (e.g., LST, NDVI, Albedo), which may affect the accuracy of downscaled SSM (Piles et al., 2011).

In this study, by comprehensively considering spatial resolution, spatial continuity, and further accuracy improvement, we proposed the GRASPS framework by integrating point-surface data fusion through advanced deep learning algorithm and pixel classification-based bias correction. The overall correlation coefficient and RMSE for the final downscaled SSM achieved 0.78 and $0.39 \text{ m}^3\text{m}^{-3}$, respectively. More significantly, our downscaled SSM were characterized by daily, gap-free data at 30 m, which was not achieved simultaneously by previous studies. Theoretically, the proposed methodology can also be transferred to other land surface variables (e.g., air temperature, evapotranspiration, precipitation) and other spatial scales (e.g., 1km, 0.1° , 0.25°). Since this study focused on the generation of SSM, the independent variables were all SSM related parameters. When the framework is applied to other land surface variables, the predictor variables can be replaced based on different situations. For instance, the fusion of air temperature can adopt more meteorological data (e.g., wind speed) or socioeconomic data (e.g., population density). Besides, the threshold in the bias correction may also vary depending on different variables and study areas. In a word, the transferability and capability of generating 3H data of GRASPS make it a promising way to obtain high-quality land surface observation towards better Earth science study.

Table 2 Comparison of the latest studies related to SSM fusion. The downscaling algorithms are multivariate statistical regression (MSR), Disaggregation based on Physical and Theoretical scale Change (DisPATCH), random forest (RF), gaussian process regression (GPR), and area-to-area regression kriging (ATARK), respectively.

Studies	Methods	Spatial Resolution	Temporal Resolution	Validation Number	PCC	RMSE
Jiang et al. (2019)	Spatial temporal fusion model	9 km	Daily	649 sites	0.55	0.109
Qu et al. (2021)	MSR/DisPATCH/RF/GPR/ATARK	0.01°	Daily	74 sites	0.45-0.56	0.117-0.137
Long et al. (2019)	Random Forest	1 km	Daily (All weather)	470 samples	0.68-0.72	0.041-0.047
Liu et al. (2020)	Six machine learning methods	1 km	Daily	99/20/57/37 sites	0.71/0.70/0.67 /0.55	0.037/0.036/0.032/0.038
Abbaszadeh et al. (2019)	Random Forest	1 km	Daily	About 300 sites	0.78	0.043
Abowarda et al. (2021)	Random Forest	30 m	Daily (All weather)	397/113 samples	0.74	0.046
Zappa et al. (2019)	Random Forest	30 m	Daily	Over 3000 samples	0.76	0.049
Our Study	GRASPS	30 m	Daily (All weather)	3376 samples	0.78	0.039

5.2 Limitations

Firstly, in order to improve the downscaling accuracy, we designed the pixel classification based bias correction method. The proposed bias correction method combined the linear correction and variance scaling. The method considered in-situ sites with relatively complete recordings as C1 pixels, which were the references of the classification of C2 and C3 pixels. In addition, the obtained correction parameters (i.e., linear correction parameter and variance scaling parameter) were used to correct the SSM time series as a whole. In this case, the proposed method was a kind of global correction method, which considered the general dynamics of downscaled SSM and in-situ SSM during the entire study period (Chen et al., 2011; Leander and Buishand, 2007). The original temporal pattern of the series would be largely retained due to the global correction and thus the different dynamics could still be seen between the corrected SSM and in-situ SSM at certain periods. To this point, a more comprehensive correction method considering both global characteristics and local characteristics of the time series still requires exploration in the future.

In this study, we proposed a framework to generate 3H SSM through deep learning method and point-surface data fusion method. On one hand, deep learning is a kind of black-box method. Although deep learning is powerful in fitting non-linear relationship and has exhibited excellent performance in various earth science studies, one major drawback is that this method fails to provide clear and in-depth physical mechanism of the results. On the other hands, the point-surface data fusion method usually brings spatial scale mismatch issue by fusing satellite/model-based data and in-situ ground measurements. It will further exert negative effects on the SSM downscaling accuracy and understanding of the underlying process. Thus, it is promising to combine the deep learning-based method and the process-based model to enhance the SSM downscaling accuracy and reveal the underlying mechanism in the future.

6. Conclusions

In this study, an integrated methodology (GRASPS), inspired by point-surface data fusion and deep learning, was proposed along with fusion of multi-source remotely sensed, model-based, and in-situ ground data sets. GRASPS was designed to generate 3H (i.e., high spatial resolution, high accuracy, high spatial-temporal continuity) SSM data and it was evaluated in a densely distributed soil moisture sensor network (HOAL network) located in Petzenkirchen, Austria. The key findings are given as follows:

(1) ESTARFM was adopted to generate high-quality inputs (i.e., NDVI, Albedo, LST) with a spatial resolution of 30 m for the subsequent fusion model. Downscaled auxiliary data was evaluated against 30 m Landsat 8 data at validation date and the comparative analysis demonstrated that the implementation of ESTARFM considerably enhanced the spatio-temporal continuity and details of spatial distribution for the downscaled SSM.

(2) DBN was adopted to downscale SSM at 30 m by fitting a total of seven SSM related predictor. The average PCC, RMSE, ubRMSE, bias, and MAE were 0.78, 0.048 m^3m^{-3} , 0.033 m^3m^{-3} , -0.001 m^3m^{-3} , and 0.041 m^3m^{-3} , respectively.

(3) In order to reduce the systematic biases and improve the accuracy of downscaled SSM, a pixel classification based bias correction method was developed. Results indicated that the RMSE, ubRMSE, bias, and MAE of the downscaled SSM at the validation sites after the bias correction were improved by 13%, 7%, 22%, and 18%, respectively.

(4) Further spatial and temporal analysis of downscaled SSM compared to ERA-5 SSM and SMAP SSM exhibited that our GRASPS-SSM can better capture the local SSM dynamics and represent more detailed spatial characteristics. Moreover, the comparative analysis confirmed the effectiveness of the deep learning algorithms and the combinations of the input variables in the GRASPS framework.

To conclude, results and comparative analysis shown in this study suggested that the proposed SSM GRASPS framework had potential in generating high resolution (e.g., 30 m) spatio-temporally continuous SSM at high accuracy. The obtained 3H SSM dataset is featured by the high resolution (30 m), high accuracy, daily resolution and cloud/gap-free. Meanwhile, the methodology is also transferrable to other land surface

variables and spatial scales. In this scenario, the predictors, collected datasets, or downscaling algorithm in GRASPS can be adjusted according to the estimated variables. As such, this proposed method could be further applied for other environmental data fusion problems.

Data Availability Statement

We appreciate United State Geological Survey (USGS) for providing Landsat 8 data (<https://landsat.gsfc.nasa.gov/landsat-8/landsat-8-overview>), Land Processes Distributed Active Archive Center (LP DAAC) for providing MOD11A1 (<https://lpdaac.usgs.gov/products/mod11a1v006/>) and MOD09GA (<https://lpdaac.usgs.gov/products/mod09gav006/>), National Aeronautics and Space Administration (NASA) for providing SMAP Level-4 product (<https://www.nasa.gov/smap/>), European Centre for Medium-Range Weather Forecasts (ECMWF) for providing ERA-5 reanalysis data (<https://www.ecmwf.int/en/forecasts/datasets/reanalysis-datasets/era5>), and International Soil Moisture Network (ISMN) for providing in-situ SSM measurements (<https://ismn.geo.tuwien.ac.at/en/>). The observed precipitation, crop management, and soil texture data were applied from the HOAL catchment (<https://hoal.hydrology.at/the-hoal>). The data in this study will be released on Zenodo which can be found at <https://doi.org/10.5281/zenodo.6321423> (Huang et al., 2022. DOI: 10.5281/zenodo.6321423).

Acknowledgement

This work was supported by grants from the National Key R&D Program (no.2018YFB2100500) and National Natural Science Foundation of China program (41801339, 41890822, 41771422, 41601406). Besides, we would like to thank Gerhard Rab for the support with the in-situ data collection for the HOAL catchment.

References

- Abbaszadeh, P., M. Hamid, & X. Zhan (2018). Downscaling SMAP Radiometer Soil Moisture over the CONUS Using an Ensemble Learning Method. *Water Resources Research*, 55. DOI:10.1029/2018WR023354
- Abowarda, A. S., L. Bai, C. Zhang, D. Long, X. Li, Q. Huang, & Z. Sun (2021). Generating surface soil moisture at 30 m spatial resolution using both data fusion and machine learning toward better water resources management at the field scale. *Remote Sensing of Environment*, 255, 112301. DOI:10.1016/j.rse.2021.112301
- Arabi, B., M. S. Salama, J. Pitarch, & W. Verhoef (2020). Integration of in-situ and multi-sensor satellite observations for long-term water quality monitoring in coastal areas. *Remote Sensing of Environment*, 239, 111632. DOI:10.1016/j.rse.2020.111632
- Bojinski, S., M. Verstraete, T. C. Peterson, C. Richter, A. Simmons, & M. Zemp (2014). The Concept of Essential Climate Variables in Support of Climate Research, Applications, & Policy. *Bulletin of the American Meteorological Society*, 95(9), 1431-1443. DOI:10.1175/bams-d-13-00047.1
- Breiman, L., 2001. Random Forests. *Machine Learning*, 45(1): 5-32. DOI:10.1023/A:1010933404324
- Brocca, L., F. Melone, T. Moramarco, & R. Morbidelli (2010). Spatial-temporal variability of soil moisture and its estimation across scales. *Water Resources Research*, 46, W02516. DOI:10.1029/2009WR008016
- Chen, D., Chen, N., Zhang, X., Ma, H., Chen, Z., 2021. Next-Generation Soil Moisture Sensor Web: High-Density In Situ Observation Over NB-IoT. *IEEE Internet of Things Journal*, 8(17): 13367-13383. DOI:10.1109/JIOT.2021.3065077
- Chen, J., F. P. Brissette, & R. Leconte (2011). Uncertainty of downscaling method in quantifying the impact of climate change on hydrology. *Journal of Hydrology*, 401(3-4), 190-202. DOI:10.1016/j.jhydrol.2011.02.020

- Chen, X., J. Parajka, B. Szeles, P. Strauss, & G. Blöschl (2020). Spatial and temporal variability of event runoff characteristics in a small agricultural catchment. *Hydrological sciences journal = Journal des sciences hydrologiques*, 65(13), 2185-2195. DOI:10.1080/02626667.2020.1798451
- Cheng, Q., H. Shen, L. Zhang, Q. Yuan, & C. Zeng (2014). Cloud removal for remotely sensed images by similar pixel replacement guided with a spatio-temporal MRF model. *ISPRS Journal of Photogrammetry and Remote Sensing*, 92, 54-68. DOI:10.1016/j.isprsjprs.2014.02.015
- Cosh, M., T. Jackson, & R. Bindlish (2004). Watershed scale temporal and spatial stability of soil moisture and its role in validating satellite estimates. *Remote Sensing of Environment*, 92, 427-435. DOI:10.1016/j.rse.2004.02.016
- Crow, W.T. et al., 2012. Upscaling sparse ground-based soil moisture observations for the validation of coarse-resolution satellite soil moisture products. *Reviews of Geophysics*, 50(2). DOI:10.1029/2011rg000372
- Cui, Y., D. Long, Y. Hong, C. Zeng, J. Zhou, Z. Han, R. Liu, & W. Wan (2016). Validation and reconstruction of FY-3B/MWRI soil moisture using an artificial neural network based on reconstructed MODIS optical products over the Tibetan Plateau. *Journal of Hydrology*, 543, 242-254. DOI:10.1016/j.jhydrol.2016.10.005
- Das, N., D. Entekhabi, E. Njoku, J. Shi, J. Johnson, & A. Colliander (2014). Tests of the SMAP Combined Radar and Radiometer Algorithm Using Airborne Field Campaign Observations and Simulated Data. *Geoscience and Remote Sensing, IEEE Transactions on*, 52, 2018-2028. DOI:10.1109/TGRS.2013.2257605
- Das, N. N., et al. (2019). The SMAP and Copernicus Sentinel 1A/B microwave active-passive high resolution surface soil moisture product. *Remote Sensing of Environment*, 233, 111380. DOI:10.1016/j.rse.2019.111380
- De Lannoy, G. J. M., & R. H. Reichle (2016). Assimilation of SMOS brightness temperatures or soil moisture retrievals into a land surface model. *Hydrology and Earth System Sciences*, 20(12), 4895-4911. DOI:10.5194/hess-20-4895-2016

- Dong, S., Wang, P., Abbas, K., 2021. A survey on deep learning and its applications. *Computer Science Review*, 40: 100379. DOI:10.1016/j.cosrev.2021.100379
- Dorigo, W., et al. (2017). ESA CCI Soil Moisture for improved Earth system understanding: State-of-the art and future directions. *Remote Sensing of Environment*, 203, 185-215. DOI:10.1016/j.rse.2017.07.001
- Dorigo, W., et al. (2021). The International Soil Moisture Network: serving Earth system science for over a decade. *Hydrol. Earth Syst. Sci. Discuss.*, 2021, 1-83. DOI:10.5194/hess-2021-2
- Entekhabi, D., et al. (2010). The Soil Moisture Active and Passive (SMAP) mission. *Proceedings of the IEEE*, 98, 704-716. DOI:10.1109/JPROC.2010.2043918
- Ford, T., & S. Quiring (2019). Comparison of Contemporary In Situ, Model, & Satellite Remote Sensing Soil Moisture With a Focus on Drought Monitoring. *Water Resources Research*, 55. DOI:10.1029/2018WR024039
- Gascoin, S., A. Ducharne, P. Ribstein, E. Perroy, & P. Wagnon (2009). Sensitivity of bare soil albedo to surface soil moisture on the moraine of the Zongo glacier (Bolivia). *Geophysical Research Letters - GEOPHYS RES LETT*, 36. DOI:10.1029/2008GL036377
- Gómez-Plaza, A., Martínez-Mena, M., Albaladejo, J., Castillo, V., 2001. Factors regulating spatial distribution of soil water content in small semiarid catchments. *Journal of Hydrology*, 253: 211-226. DOI:10.1016/S0022-1694(01)00483-8
- Gu, X., Q. Zhang, J. Li, V. P. Singh, J. Liu, P. Sun, C. He, & J. Wu (2019). Intensification and Expansion of Soil Moisture Drying in Warm Season Over Eurasia Under Global Warming. *Journal of Geophysical Research: Atmospheres*, 124(7), 3765-3782. DOI:https://doi.org/10.1029/2018JD029776
- Heathman, G., M. Cosh, E. Han, T. Jackson, L. McKee, & S. McAfee (2012). Field scale spatiotemporal analysis of surface soil moisture for evaluating point-scale in situ networks. *Geoderma*, 170, 195 – 205. DOI:10.1016/j.geoderma.2011.11.004
- Hersbach, H., et al. (2020). The ERA5 global reanalysis. *Quarterly Journal of the Royal Meteorological Society*, 146(730), 1999-2049. DOI:10.1002/qj.3803

- Hinton, G., S. Osindero, & Y.-W. Teh (2006). A Fast Learning Algorithm for Deep Belief Nets. *Neural computation*, 18, 1527-1554. DOI:10.1162/neco.2006.18.7.1527
- Hu, F., Z. Wei, W. Zhang, D. Dorjee, & L. Meng (2020). A spatial downscaling method for SMAP soil moisture through visible and shortwave-infrared remote sensing data. *Journal of Hydrology*, 590, 125360. DOI:10.1016/j.jhydrol.2020.125360
- Huang, S., X. Zhang, N. Chen, B. Li, H. Ma, L. Xu, R. Li, & D. Niyogi (2021). Drought propagation modification after the construction of the Three Gorges Dam in the Yangtze River Basin. *Journal of Hydrology*, 603, 127138. DOI:10.1016/j.jhydrol.2021.127138
- Huang S., et al. (2022). Generating high Resolution Accurate Seamless data using Point Surface fusion (Version 1.0) [Data set]. Zenodo. <http://doi.org/10.5281/zenodo.6321423>
- Hupet, F., Vanclooster, M., 2002. Interseasonal Dynamics of Soil Moisture Variability Within a Small Agricultural Maize Cropped Field. *Journal of Hydrology*, 261: 86-101. DOI:10.1016/S0022-1694(02)00016-1
- Jiang, H., S. Huanfeng, L. Xinghua, Z. Chao, L. Huiqin, & L. Fangni (2019). Extending the SMAP 9-km soil moisture product using a spatio-temporal fusion model. *Remote Sensing of Environment*, 231, 111224. DOI:10.1016/j.rse.2019.111224
- Jing, W., P. Zhang, & X. Zhao (2018). Reconstructing Monthly ECV Global Soil Moisture with an Improved Spatial Resolution. *Water Resources Management*, 32(7), 2523-2537. DOI:10.1007/s11269-018-1944-2
- Kathuria, D., B. Mohanty, & M. Katzfuss (2019), Multiscale Data Fusion for Surface Soil Moisture Estimation: A Spatial Hierarchical Approach.
- Kerr, Y., et al. (2010). The SMOS Mission: New Tool for Monitoring Key Elements of the Global Water Cycle. *Proceedings of the IEEE*, 98. DOI:10.1109/JPROC.2010.2043032
- Kim, H., et al. (2020). Global scale error assessments of soil moisture estimates from microwave-based active and passive satellites and land surface models over forest and mixed irrigated/dryland agriculture regions. *Remote Sensing of*

- Environment, 251, 112052. DOI:10.1016/j.rse.2020.112052
- Kolassa, J., et al. (2017). Estimating surface soil moisture from SMAP observations using a Neural Network technique. *Remote Sensing of Environment*, 204. DOI:10.1016/j.rse.2017.10.045
- Koster, R. D., et al. (2004). Regions of Strong Coupling Between Soil Moisture and Precipitation. *Science*, 305(5687), 1138-1140. DOI:10.1126/science.1100217
- Leander, R., & T. A. Buishand (2007). Resampling of regional climate model output for the simulation of extreme river flows. *Journal of Hydrology*, 332(3-4), 487-496. DOI:10.1016/j.jhydrol.2006.08.006
- Leng, P., Z.-L. Li, S.-B. Duan, M. Gao, & H.-Y. Huo (2017). A practical approach for deriving all-weather soil moisture content using combined satellite and meteorological data. *ISPRS Journal of Photogrammetry and Remote Sensing*, 131. DOI:10.1016/j.isprsjprs.2017.07.013
- Li, K., Zhang, J., Wu, L., 2018. Assessment of Soil Moisture - Temperature Feedbacks With the CCSM - WRF Model System Over East Asia. *Journal of Geophysical Research: Atmospheres*, 123(13): 6822-6839. DOI:10.1029/2017jd028202
- Li, K., Zhang, J., Yang, K., Wu, L., 2019. The Role of Soil Moisture Feedbacks in Future Summer Temperature Change over East Asia. *Journal of Geophysical Research: Atmospheres*, 124(22): 12034-12056. DOI:10.1029/2018jd029670
- Li, T., H. Shen, Q. Yuan, X. Zhang, & L. Zhang (2017). Estimating Ground-Level PM_{2.5} by Fusing Satellite and Station Observations: A Geo-Intelligent Deep Learning Approach. *Geophysical Research Letters*, 44(23), 11,985-911,993. DOI:10.1002/2017gl075710
- Li, J., S. Wang, G. Gunn, P. Joosse, & H. A. J. Russell (2018). A model for downscaling SMOS soil moisture using Sentinel-1 SAR data. *International Journal of Applied Earth Observation and Geoinformation*, 72, 109-121. DOI:10.1016/j.jag.2018.07.012
- Li, R., T. Huang, Y. Song, S. Huang, & X. Zhang (2021a). Generating 1 km Spatially Seamless and Temporally Continuous Air Temperature Based on Deep Learning over Yangtze River Basin, China. *Remote Sensing*, 13(19).

DOI:10.3390/rs13193904

- Li, Q., Z. Wang, W. Shangguan, L. Li, Y. Yao, & F. Yu (2021b). Improved Daily SMAP Satellite Soil Moisture Prediction over China using deep learning model with transfer learning. *Journal of Hydrology*, 600, 126698. DOI:10.1016/j.jhydrol.2021.126698
- Lievens, H., et al. (2016). Assimilation of SMOS soil moisture and brightness temperature products into a land surface model. *Remote Sensing of Environment*, 180, 292-304. DOI:10.1016/j.rse.2015.10.033
- Lin, W.-C., Tsai, C.-F., Zhong, J.R., 2022. Deep learning for missing value imputation of continuous data and the effect of data discretization. *Knowledge-Based Systems*, 239: 108079. DOI:10.1016/j.knosys.2021.108079
- Liu, P.-W. et al., 2021. Assessing Disaggregated SMAP Soil Moisture Products in the United States. *IEEE Journal of Selected Topics in Applied Earth Observations and Remote Sensing*, PP: 1-1. DOI:10.1109/JSTARS.2021.3056001
- Liu, Y., W. Jing, Q. Wang, & X. Xia (2020). Generating high-resolution daily soil moisture by using spatial downscaling techniques: a comparison of six machine learning algorithms. *Advances in Water Resources*, 141, 103601. DOI:10.1016/j.advwatres.2020.103601
- Liu, Y., L. Yao, W. Jing, L. Di, J. Yang, & Y. Li (2020). Comparison of two satellite-based soil moisture reconstruction algorithms: A case study in the state of Oklahoma, USA. *Journal of Hydrology*, 590, 125406. DOI:10.1016/j.jhydrol.2020.125406
- Long, D., L. Bai, L. Yan, C. Zhang, W. Yang, H. Lei, J. Quan, X. Meng, & C. Shi (2019). Generation of spatially complete and daily continuous surface soil moisture of high spatial resolution. *Remote Sensing of Environment*, 233, 111364. DOI:10.1016/j.rse.2019.111364
- Ma, H., J. Zeng, N. Chen, Z. Xiang, M. Cosh, & W. Wang (2019). Satellite surface soil moisture from SMAP, SMOS, AMSR2 and ESA CCI: A comprehensive assessment using global ground-based observations. *Remote Sensing of Environment*, 231C, 111215. DOI:10.1016/j.rse.2019.111215

- Markham, B. L., & D. L. Helder (2012). Forty-year calibrated record of earth-reflected radiance from Landsat: A review. *Remote Sensing of Environment*, 122, 30-40. DOI:10.1016/j.rse.2011.06.026
- Malbêteau, Y., Merlin, O., Molero, B., Rüdiger, C., Bacon, S., 2016. DisPATCH as a tool to evaluate coarse-scale remotely sensed soil moisture using localized in situ measurements: Application to SMOS and AMSR-E data in Southeastern Australia. *International Journal of Applied Earth Observation and Geoinformation*, 45: 221-234. DOI:10.1016/j.jag.2015.10.002
- McColl, K. A., S. H. Alemohammad, R. Akbar, A. G. Konings, S. Yueh, & D. Entekhabi (2017). The global distribution and dynamics of surface soil moisture. *Nature Geoscience*, 10(2), 100-104. DOI:10.1038/ngeo2868
- Montzka, C., T. Jagdhuber, R. Horn, H. Bogen, I. Hajnsek, A. Reigber, & H. Vereecken (2016). Investigation of SMAP Fusion Algorithms With Airborne Active and Passive L-Band Microwave Remote Sensing. *IEEE Transactions on Geoscience and Remote Sensing*, 54, 1-12. DOI:10.1109/TGRS.2016.2529659
- Njoku, E., T. Jackson, V. Lakshmi, T. Chan, & S. Nghiem (2003). Soil moisture retrieval from AMSR-E. *Geoscience and Remote Sensing, IEEE Transactions on*, 41, 215-229. DOI:10.1109/TGRS.2002.808243
- Peng, J., A. Loew, O. Merlin, & N. Verhoest (2017). A review of spatial downscaling of satellite remotely sensed soil moisture. *Reviews of Geophysics*, 55. DOI:10.1002/2016RG000543
- Peng, J., et al. (2021). A roadmap for high-resolution satellite soil moisture applications – confronting product characteristics with user requirements. *Remote Sensing of Environment*, 252, 112162. DOI:10.1016/j.rse.2020.112162
- Pfeil, I., M. Vreugdenhil, S. Hahn, W. Wagner, P. Strauss, & G. Blöschl (2018). Improving the Seasonal Representation of ASCAT Soil Moisture and Vegetation Dynamics in a Temperate Climate. *Remote Sensing*, 10(11), 1788. DOI:10.3390/rs10111788
- Piles, M., A. Camps, M. Vall-llossera, I. Corbella, R. Panciera, C. Rüdiger, Y. Kerr, & J. Walker (2011). Downscaling SMOS-derived soil moisture using MODIS

- Visible/Infrared data. *Geoscience and Remote Sensing, IEEE Transactions on*, 49, 3156-3166. DOI:10.1109/TGRS.2011.2120615
- Qu, Y., et al. (2021). Inter-comparison of several soil moisture downscaling methods over the Qinghai-Tibet Plateau, China. *Journal of Hydrology*, 592, 125616. DOI:10.1016/j.jhydrol.2020.125616
- Qu, Y., et al. (2019). Rebuilding a Microwave Soil Moisture Product Using Random Forest Adopting AMSR-E/AMSR2 Brightness Temperature and SMAP over the Qinghai - Tibet Plateau, China. *Remote Sensing*, 11(6), 683. DOI:10.3390/rs11060683
- Reichle, R. H., et al. (2017). Global Assessment of the SMAP Level-4 Surface and Root-Zone Soil Moisture Product Using Assimilation Diagnostics. *Journal of hydrometeorology*, 18(12), 3217-3237. DOI:10.1175/JHM-D-17-0130.1
- Rumelhart, D., Hinton, G., Williams, R., 1986. Learning Representations by Back Propagating Errors. *Nature*, 323: 533-536. DOI:10.1038/323533a0
- Sabaghy, S., J. Walker, L. Renzullo, & T. Jackson (2018). Spatially enhanced passive microwave derived soil moisture: Capabilities and opportunities. *Remote Sensing of Environment*, 209, 551-580. DOI:10.1016/j.rse.2018.02.065
- Senanayake, I. P., I. Y. Yeo, N. Tangdamrongsub, G. R. Willgoose, G. R. Hancock, T. Wells, B. Fang, V. Lakshmi, & J. P. Walker (2019). An in-situ data based model to downscale radiometric satellite soil moisture products in the Upper Hunter Region of NSW, Australia. *Journal of Hydrology*, 572, 820-838. DOI:10.1016/j.jhydrol.2019.03.014
- Shen, G., N. Chen, W. Wang, & Z. Chen (2019). WHU-SGCC: a novel approach for blending daily satellite (CHIRP) and precipitation observations over the Jinsha River basin. *Earth System Science Data*, 11(4), 1711-1744. DOI:10.5194/essd-11-1711-2019
- Shen, H., Y. Jiang, T. Li, Q. Cheng, C. Zeng, & L. Zhang (2020). Deep learning-based air temperature mapping by fusing remote sensing, station, simulation and socioeconomic data. *Remote Sensing of Environment*, 240, 111692. DOI:10.1016/j.rse.2020.111692

- Song, P., Y. Zhang, & J. Tian (2021). Improving Surface Soil Moisture Estimates in Humid Regions by an Enhanced Remote Sensing Technique. *Geophysical Research Letters*, 48(5). DOI:10.1029/2020gl091459
- Széles, B., J. Parajka, P. Hogan, R. Silasari, L. Pavlin, P. Strauss, & G. Blöschl (2021). Stepwise prediction of runoff using proxy data in a small agricultural catchment. *Journal of Hydrology and Hydromechanics*, 69(1), 65-75. DOI:10.2478/johh-2020-0029
- Tagesson, T., S. Horion, H. Nieto, V. Fornies, G. Mendiguren González, C. Bulgin, D. Ghent, & R. Fensholt (2018). Disaggregation of SMOS soil moisture over West Africa using the Temperature and Vegetation Dryness Index based on SEVIRI land surface parameters. *Remote Sensing of Environment*, 206, 424-441. DOI:10.1016/j.rse.2017.12.036
- Tiefenbacher, A., G. Weigelhofer, A. Klik, L. Mabit, J. Santner, W. Wenzel, & P. Strauss (2021). Antecedent soil moisture and rain intensity control pathways and quality of organic carbon exports from arable land. *Catena*, 202, 105297. DOI:10.1016/j.catena.2021.105297
- Vergopolan, N., N. W. Chaney, H. E. Beck, M. Pan, J. Sheffield, S. Chan, & E. F. Wood (2020). Combining hyper-resolution land surface modeling with SMAP brightness temperatures to obtain 30-m soil moisture estimates. *Remote Sensing of Environment*, 242, 111740. DOI:10.1016/j.rse.2020.111740
- Wagner, W., et al. (2013). The ASCAT Soil Moisture Product: A Review of its Specifications, Validation Results, & Emerging Applications. *Meteorologische Zeitschrift*, 22, 5-33. DOI:10.1127/0941-2948/2013/0399
- Wang, S., Zhang, X., Chen, N., Wang, W., 2022. Classifying diurnal changes of cyanobacterial blooms in Lake Taihu to identify hot patterns, seasons and hotspots based on hourly GOCI observations. *Journal of environmental management*, 310: 114782. DOI:10.1016/j.jenvman.2022.114782
- Wang, Y., J. Peng, X. Song, P. Leng, R. Ludwig, & A. Loew (2018). Surface Soil Moisture Retrieval Using Optical/Thermal Infrared Remote Sensing Data. *IEEE Transactions on Geoscience and Remote Sensing*, PP, 1-10.

DOI:10.1109/TGRS.2018.2817370

- Wang, X., H. Lü, W. T. Crow, Y. Zhu, Q. Wang, J. Su, J. Zheng, & Q. Gou (2021). Assessment of SMOS and SMAP soil moisture products against new estimates combining physical model, a statistical model, & in-situ observations: A case study over the Huai River Basin, China. *Journal of Hydrology*, 598, 126468. DOI:10.1016/j.jhydrol.2021.126468
- Wang, M., Z. Zhang, T. Hu, W. g. Wang guizhou, G. He, Z. Zhang, H. Li, Z. Wu, & L. X.G (2020). An Efficient Framework for Producing Landsat-Based Land Surface Temperature Data Using Google Earth Engine. *IEEE Journal of Selected Topics in Applied Earth Observations and Remote Sensing*, PP, 1-1. DOI:10.1109/JSTARS.2020.3014586
- Wei, Z., Y. Meng, W. Zhang, J. Peng, & L. Meng (2019). Downscaling SMAP soil moisture estimation with gradient boosting decision tree regression over the Tibetan Plateau. *Remote Sensing of Environment*, 225, 30-44. DOI:10.1016/j.rse.2019.02.022
- Wigneron, J.-P., X. Li, F. Frappart, L. Fan, A. Al-Yaari, G. De Lannoy, X. Liu, W. Mengjia, E. Masson, & C. Moisy (2021). SMOS-IC data record of soil moisture and L-VOD: Historical development, applications and perspectives. *Remote Sensing of Environment*, 254, 112238. DOI:10.1016/j.rse.2020.112238
- Wilson, D., Western, A., Grayson, R., 2004. Identifying and quantifying sources of variability in temporal and spatial soil moisture observations. *Water Resources Research*, 40. DOI:10.1029/2003WR002306
- Wu, H., Q. Yang, J. Liu, & G. Wang (2020). A spatiotemporal deep fusion model for merging satellite and gauge precipitation in China. *Journal of Hydrology*, 584, 124664. DOI:10.1016/j.jhydrol.2020.124664
- Xaver, A., L. Zappa, G. Rab, I. Pfeil, M. Vreugdenhil, D. Hemment, & W. A. Dorigo (2020). Evaluating the suitability of the consumer low-cost Parrot Flower Power soil moisture sensor for scientific environmental applications. *Geoscientific Instrumentation, Methods and Data Systems*, 9(1), 117-139. DOI:10.5194/gi-9-117-2020

- Xu, H., Q. Yuan, T. Li, H. Shen, L. Zhang, & H. Jiang (2018). Quality Improvement of Satellite Soil Moisture Products by Fusing with In-Situ Measurements and GNSS-R Estimates in the Western Continental U.S. *Remote Sensing*, 10(9), 1351. DOI:10.3390/rs10091351
- Xu, L., N. Chen, X. Zhang, H. Moradkhani, C. Zhang, & C. Hu (2021). In-situ and triple-collocation based evaluations of eight global root zone soil moisture products. *Remote Sensing of Environment*, 254, 112248. DOI:10.1016/j.rse.2020.112248
- Yang, Y., J. Dong, X. Sun, E. Lima, Q. Mu, & X. Wang (2017). A CFCC-LSTM Model for Sea Surface Temperature Prediction. *IEEE Geoscience and Remote Sensing Letters*, 15, 1-5. DOI:10.1109/LGRS.2017.2780843
- Yang, G., H. Shen, W. Sun, J. Li, N. Diao, & Z. He (2018). On the Generation of Gapless and Seamless Daily Surface Reflectance Data. *IEEE Transactions on Geoscience and Remote Sensing*, PP, 1-18. DOI:10.1109/TGRS.2018.2810271
- Yao, P., H. Lu, J. Shi, T. Zhao, K. Yang, M. H. Cosh, D. J. S. Gianotti, & D. Entekhabi (2021). A long term global daily soil moisture dataset derived from AMSR-E and AMSR2 (2002-2019). *Scientific data*, 8(1), 143. DOI:10.1038/s41597-021-00925-8
- Yuan, Q., H. Xu, T. Li, H. Shen, & L. Zhang (2020a). Estimating surface soil moisture from satellite observations using a generalized regression neural network trained on sparse ground-based measurements in the continental U.S. *Journal of Hydrology*, 580, 124351. DOI:10.1016/j.jhydrol.2019.124351
- Yuan, Q., et al. (2020b). Deep learning in environmental remote sensing: Achievements and challenges. *Remote Sensing of Environment*, 241, 111716. DOI:10.1016/j.rse.2020.111716
- Zappa, L., M. Forkel, A. Xaver, & W. Dorigo (2019). Deriving Field Scale Soil Moisture from Satellite Observations and Ground Measurements in a Hilly Agricultural Region. *Remote Sensing*, 11(22), 2596. DOI:10.3390/rs11222596
- Zhang, J., Dong, W., 2010. Soil moisture influence on summertime surface air temperature over East Asia. *Theoretical and Applied Climatology*, 100: 221-226.

DOI:10.1007/s00704-009-0236-4

Zhang, X., & N. Chen (2016). Reconstruction of GF-1 Soil Moisture Observation Based on Satellite and In Situ Sensor Collaboration Under Full Cloud Contamination. *IEEE Transactions on Geoscience and Remote Sensing*, 54, 1-18.

DOI:10.1109/TGRS.2016.2558109

Zhang, X., J. Zhou, S. Liang, & D. Wang (2021). A practical reanalysis data and thermal infrared remote sensing data merging (RTM) method for reconstruction of a 1-km all-weather land surface temperature. *Remote Sensing of Environment*, 260, 112437. DOI:10.1016/j.rse.2021.112437

Zhang, X., N. Chen, Z. Chen, L. Wu, X. Li, L. Zhang, L. Di, J. Gong, & D. Li (2018). Geospatial sensor web: A cyber-physical infrastructure for geoscience research and application. *Earth-Science Reviews*, 185.

DOI:10.1016/j.earscirev.2018.07.006

Zhang, Y. et al., 2016. Multi-decadal trends in global terrestrial evapotranspiration and its components. *Scientific reports*, 6: 19124. DOI:10.1038/srep19124

Zhu, W., S. Jia, & A. Lv (2017). A time domain solution of the Modified Temperature Vegetation Dryness Index (MTVDI) for continuous soil moisture monitoring. *Remote Sensing of Environment*, 200, 1-17. DOI:10.1016/j.rse.2017.07.032

Zhu, X., J. Chen, F. Gao, X. Chen, & J. G. Masek (2010). An enhanced spatial and temporal adaptive reflectance fusion model for complex heterogeneous regions. *Remote Sensing of Environment*, 114(11), 2610-2623.

DOI:10.1016/j.rse.2010.05.032